Numerical computation of advection and diffusion on evolving diffuse interfaces

Charles M. Elliott [*], Björn Stinner [*], Vanessa Styles [†], Richard Welford [†]

Dedicated to the memory of A. R. Mitchell, 1921–2007.

Abstract

We propose a numerical method for computing transport and diffusion on a moving surface. The approach is based on a diffuse interface model in which a bulk diffusion-advection equation is solved on a layer of thickness ε containing the surface. The conserved quantity in the bulk domain is the concentration weighted by a density which vanishes on the boundary of the thin domain. Such a density arises naturally in double obstacle phase field models. The discrete equations are then formulated on a moving narrow band consisting of grid points on a fixed mesh. We show that the discrete equations are solvable subject to a natural constraint on the evolution of the discrete narrow band. Mass is conserved and the discrete solution satisfies stability bounds. Numerical experiments indicate that the method is second order accurate in space.

1 Introduction

Increasingly in applications, models feature partial differential equations on surfaces. In particular, conserved surface quantities subject to advection-diffusion equations on moving hypersurfaces may arise in areas ranging from fluid dynamics (surfactants on fluid-fluid interfaces, [2, 33]) over biological systems (lipids on biomembranes, [36, 26]) to materials science (species diffusion along grain boundaries, [29, 17, 39]). Thus developing numerical methods for surface partial differential equations is an important topic in computational mathematics. In this article we present a computational approach for an advection diffusion equation on a given moving hypersurface which is based on a diffuse interface representation of the surface.
Denoting by $\{\Gamma(t)\}_t$ an evolving hypersurface the pde

$$\partial_t u_s + \boldsymbol{v}_s \cdot \nabla u_s + u_s \nabla_\Gamma \cdot \boldsymbol{v}_s - \mathcal{D}_c \Delta_\Gamma u_s = f_s \quad \text{on } \Gamma \tag{1.1}$$

models advection and diffusion of a surface conserved quantity u_s, see [22]. The given vector field $\boldsymbol{v}_s$ is the velocity which splits in the form $\boldsymbol{v}_s = V_s \boldsymbol{\nu}_s + \boldsymbol{v}_{s,\boldsymbol{\tau}}$ into a normal part $V_s \boldsymbol{\nu}_s$ describing the geometric motion of Γ and a tangential part $\boldsymbol{v}_{s,\boldsymbol{\tau}}$ associated with the transport of material along the surface. The operator ∇_Γ is the surface gradient,

[*] Mathematics Institute and Centre for Scientific Computing, University of Warwick, Coventry, CV4 7AL, UK.

[†] Department of Mathematics, University of Sussex, Brighton, BN1 9RF, UK.

and $\Delta_\Gamma = \nabla_\Gamma \cdot \nabla_\Gamma$ is the Laplace Beltrami operator. The function f_s on the right hand side is a source term and $\mathcal{D}_c > 0$ is a constant diffusivity parameter.
The approach presented in this paper is based on representing the moving hypersurface in form of an evolving thin interfacial layer $\{\Gamma_\varepsilon(t)\}_t$ involving a small parameter ε related to its thickness. For this purpose we consider a family of non-negative, differentiable functions $\rho(\varepsilon, \cdot)$ which, when scaled with $\frac{1}{\varepsilon}$, approximate the delta distribution of the moving surface as $\varepsilon \to 0$. The evolving diffuse interface $\Gamma_\varepsilon(t)$ is then defined to be the spatial support of the $\rho(\varepsilon, \cdot)$. Our goal is now to solve the parabolic equation for a bulk quantity u

$$\partial_t(\rho u) + \nabla \cdot (\rho u \boldsymbol{v}) - \nabla \cdot \big(\mathcal{D}_c \rho \nabla u\big) = \rho f \quad \text{on } \Gamma_\varepsilon \tag{1.2}$$

which involves degenerating coefficients since ρ vanishes on $\partial\Gamma_\varepsilon$. The conserved bulk quantity ρu is transported with an appropriate extension $\boldsymbol{v}$ of the velocity field $\boldsymbol{v}_s$, and also the source term f_s is extended to a suitable function f away from the moving surface Γ. As analysed in [25] for curves and sketched for hypersurfaces in higher dimension, the equation (1.2) indeed approximates the surface equation (1.1) as $\varepsilon \to 0$.
The diffuse interface approach is motivated by both modelling and numerics. We have in mind the following two situations:

(a) In many applications the evolving surface is unknown. The phase field methodology is a powerful tool to model free boundary problems. In this approach the surface is a thin diffuse interfacial layer of width $\mathcal{O}(\varepsilon)$ across which a phase field variable φ has a steep transition from the bulk values $\approx \pm 1$ on either side of the interface e.g., see [13, 11]. Diffuse interface approximations with compact support naturally occur when the diffuse interface motion is given by the double obstacle phase field model, [9, 11] for which the bulk values of φ are identically ± 1. This leads to a sharp diffuse interface front tracking method, [28, 15]. In this context, it is natural to formulate a diffuse interface equation of the form (1.2) with

$$\rho := \sigma(\varphi) \quad \text{where } \sigma(r) = 1 - r^2. \tag{1.3}$$

Defining ρ in terms of this phase field variable in our approach enables the solution of equations on the surface in such a model. We remark that a degenerate equation of the form (1.2) appeared in a phase field model of diffusion induced grain boundary motion [29, 17].

(b) On the other hand, the use of diffuse interfaces without compact support for the numerical solution of partial differential equations on stationary surfaces was proposed by [44]. In [47] a narrow band approximation analogous to our method but only for stationary interfaces is proposed, based on choosing ρ to be the characteristic function of Γ_ε. In this context we suppose that each surface $\Gamma(t)$ is known as the zero level set of some given function $d(\boldsymbol{x}, t)$ (which may be the signed distance function) and we choose to take

$$\rho(\varepsilon, \boldsymbol{x}, t) := \sigma(d(\boldsymbol{x}, t)/\varepsilon) \tag{1.4}$$

in (1.2) where $\sigma(r) > 0$ if $|r| < \alpha_w$ and $\sigma(r) = 0$ if $|r| \geq \alpha_w$ with a constant $\alpha_w > 0$.

Let us briefly discuss other methods to solve surface pdes:

- One may use finite elements on triangulated hypersurfaces as proposed and analysed for the Laplace-Beltrami equation by [18]. This surface finite element method (SFEM) is a powerful approach which has been extended to parabolic equations on stationary surfaces, including nonlinear and higher order equations, in [20]. In order to treat diffusion and transport on moving surfaces, [19] proposed the evolving surface finite element method (ESFEM). The basis for this was the use of a transport equation which in the variational setting avoided the calculation of surface quantities such as the normal, mean curvature and normal velocity. The method simply requires the velocity of the vertices of the triangulation. An application to a complex physical model may be found in [23]. In contrast, the bulk equation (1.2) may be solved on a bulk mesh, independent of $\Gamma(t)$, where it is sufficient to perform calculations belonging to the thin interfacial layer.

- Another approach involving bulk equations is to solve the surface partial differential equation on all level sets of a prescribed function. This is inherently an Eulerian method and yields degenerate equations, see [7, 32, 31, 21] for stationary surfaces. Eulerian approaches to transport and diffusion on evolving surfaces were given in [2, 52] where level set approximations to surface quantities were required. On the other hand an elegant formulation avoiding the need to do this was provided in [22] using an implicit surface version of the transport equation. This is a particularly appealing approach when the surface is computed using a level set method [48, 43]. In which case it is natural to exploit the implicit formulation and use a bulk triangulation rather than generating a surface triangulation approximating the interface from the level set function. In the stationary case the calculations in this approach can be restricted to a narrow band around the zero level set defining the interface. For surface elliptic equations, [16] gave a discretisation error analysis for a narrow band level set method using the unfitted finite element method, [3, 4], yielding an $\mathcal{O}(h)$ error in the $H^1(\Gamma)$ norm. Computations for physical models using this approach may be found in [49, 50].

- An interesting development of the implicit surface approach is to solve the equation on the zero level set of a discrete level set function on a bulk mesh which is independent of the surface, [42, 41].

- The closest point method, [45, 37, 38], is based on considering $u(\boldsymbol{a}(\boldsymbol{x}))$ where $\boldsymbol{a}(\boldsymbol{x}) \in \Gamma$ is the point closest to $\boldsymbol{x}$ and which is unique for $\boldsymbol{x}$ in a sufficiently small neighbourhood $\mathcal{U}$ of the surface Γ. The surface partial differential equation is then embedded and discretised in $\mathcal{U}$ using $u(\boldsymbol{a}(\boldsymbol{x}))$. Implementation requires the knowledge or calculation of the closest point $\boldsymbol{a}(\boldsymbol{x})$. In the cited references this approach has been used to solve a wide variety of equations on stationary surfaces.

Our approach is to approximate weak solutions to (1.2) using linear finite elements in space and a backward Euler scheme for the discretisation in time. The given functions ρ and $\boldsymbol{v}$ are projected to the finite element space for this purpose, and the mass matrix is lumped. We observe the following about our scheme:

1. The solvability of the discrete linear system of equations is not straightforward because of the degeneracy of the coefficients. The idea is to restrict the set of equations to the vertices that lie in or are connected to the diffuse interfacial

layer. On the vertices at the boundary of the diffuse interface the weight function ρ still vanishes so that there is no contribution to the ρ weighted mass matrix. However thanks to the positivity of $\mathcal{D}_c$ there is a contribution to the stiffness matrix which allows the computation of u in such boundary vertices.

2. It turns out that the degeneracy of ρ on the boundary of Γ_ε, together with a restriction on the time step for the solvability, keeps the mass on the surface during the evolution, ensuring that the total mass is preserved.

3. We computationally investigate the convergence behaviour for a prescribed moving surface in the situation (a) as specified above. For fixed ε, the numerical tests indicate a quadratic convergence in L^2 and L^∞ and a linear convergence in H^1 as the grid parameter h tends to zero, which is what one would expect when using linear finite elements. Of further interest is the convergence behaviour in ε. When keeping the ratio ε/h fixed we observed quadratic convergence in L^2 and L^∞ and linear convergence in H^1 as $\varepsilon \to 0$. Our convergence results for stationary surfaces with respect to ε and h agree with the results in [47] in spite of the different ρ.

The structure of the article is as follows. In the next section we introduce the numerical scheme. In section 3 we present numerical results for situation (b). Finally, in section 4 we present some simulation results in situation (a) for applications where the movement of the interface is not given but subject to equations of phase field type. For the numerical simulations, the finite element toolbox ALBERTA, [46], has been used.

2 Finite element approximation

2.1 Weak formulation

Let $I := [0, t_f)$ with $t_f > 0$ be a time interval and let $\Omega \subset \mathbb{R}^d$, $d = 2, 3$, denote an appropriate domain into which the evolving closed hypersurface $\Gamma(t)$ is embedded at all times. The function $\rho : (0, \varepsilon_0) \times \Omega_I \to \mathbb{R}$ (where $\Omega_I := \Omega \times I$) is such that its support $\Gamma_\varepsilon(t)$ contains Γ and converges to Γ as $\varepsilon \to 0$ with respect to the Hausdorff distance. We assume that ρ is continuously differentiable with respect to time and space so that, in particular, $\rho(\varepsilon, \boldsymbol{x}, t) \to 0$ and $\nabla\rho(\varepsilon, \boldsymbol{x}, t) \to 0$ as $(\boldsymbol{x}, t)$ approaches the boundary of $\Gamma_\varepsilon(t)$. Initial values for (1.1), denoted by u_s^0, are extended constantly in the normal direction away from Γ to obtain initial values u^0 for (1.2) on $\Gamma_\varepsilon(0)$ (we assume here that ε_0 is small enough to ensure that this extension is well-defined). On $\Omega \backslash \Gamma_\varepsilon(0)$ we set $u^0 = 0$.

Definition 2.1. (Weak solution) For a given $\varepsilon \in (0, \varepsilon_0)$, a function $u : \Omega \times [0, t_f) \to \mathbb{R}$ with $u(\boldsymbol{x}, t) = 0$ if $\boldsymbol{x} \notin \Gamma_\varepsilon(t)$ is a weak solution to (1.2) if it fulfils

$$\int_\Omega (\partial_t(\rho u)\chi - \rho u\, \boldsymbol{v} \cdot \nabla\chi + \mathcal{D}_c \rho \nabla u \cdot \nabla\chi) dx = \int_\Omega \rho f \chi dx \quad \text{a.e.} \quad t \in I \tag{2.1}$$

for all test functions $\chi : \Omega \to \mathbb{R}$ and if $u(\cdot, 0) = u^0(\cdot)$ on Ω.

2.2 Discrete setup

Let $\Delta t := \frac{t_f}{N_f}$ for an integer $N_f \in \mathbb{N}$ be a timestep and define $t_n := n\Delta t$, $n = 0, ..., N_f$. Function evaluations or approximations of functions at time t_n will be denoted with an

upper index n. The discrete time derivative is defined by

$$\delta_t f^n := \frac{f^{n+1} - f^n}{\Delta t}.$$

Let $\mathcal{T}_h$ be a triangulation of the domain $\Omega \subset \mathbb{R}^d, d = 2, 3$ consisting of simplices with maximal diameter $h := \max_{e \in \mathcal{T}_h} \operatorname{diam}(e)$. Let N be the number and $\mathcal{N}$ be the set of vertex indices. The vertex coordinates are denoted by $\{\boldsymbol{a}_1, ..., \boldsymbol{a}_N\}$. For an index $i \in \mathcal{N}$ let ω_i denote the neighbouring vertices connected to vertex i via an edge and let $\mathcal{T}_i := \{e \in \mathcal{T}_h \mid \boldsymbol{a}_i \in e\}$ be the set of elements which have i as a vertex. Further, let $\mathcal{N}_e := \{j \in \mathcal{N} \mid \boldsymbol{a}_j \in e\}$ be the set of vertices belonging to an element $e \in \mathcal{T}_h$.

Definition 2.2. The **discrete interface** at time t_n is defined by

$$\Gamma_h^n := \{e \in \mathcal{T}_h \,|\, \mathcal{N}_e \subset \mathcal{N}_h^n\}$$

where

$$\mathcal{N}_h^n := \{i \in \mathcal{N} | \text{ there is } j \in \omega_i \text{ such that } \rho^n(\boldsymbol{a}_j) > 0\}.$$

We also split the index set as follows:

$$\mathcal{N}_h^n = \mathcal{N}_{I,h}^n \cup \mathcal{N}_{B,h}^n, \quad \mathcal{N}_{I,h}^n := \{i \in \mathcal{N}_h^n |\ \rho^n(\boldsymbol{a}_i) > 0\}, \quad \mathcal{N}_{B,h}^n := \{i \in \mathcal{N}_h^n |\ \rho^n(\boldsymbol{a}_i) = 0\}.$$

Assumption 2.3. (Discrete interface assumption)
It holds for all $n = 0, \ldots, N_f - 1$ that
if an index $i \in \mathcal{N}_h^n$ does not belong to $\mathcal{N}_h^{n+1}$ then $\rho^n(\boldsymbol{a}_i) = 0$ (i.e. $i \in \mathcal{N}_{B,h}^n$).

This assumption implies that the discrete narrow band Γ_h^n never loses a whole element of the fixed mesh in a single timestep. To guarantee the above restriction one may apply an adaptive time stepping strategy or apply a condition of the form $\Delta t \leq Ch/(||\boldsymbol{v}||_{\infty,\Omega_I})$. The discrete finite element space is defined by

$$\mathcal{S}^h := \{v_h \in C^0(\bar{\Omega}) \,|\, v_h \text{ is a linear polynomial on each } e \in \mathcal{T}_h\}.$$

The interpolation operator $\Pi^h : C(\bar{\Omega}) \to \mathcal{S}^h$ is defined by

$$\Pi^h(\eta) := \sum_{i=1}^{N} \eta(\boldsymbol{a}_i)\chi_i.$$

By $\chi_1, ..., \chi_N$ we denote the standard basis functions of $\mathcal{S}^h$, i.e., $\chi_i \in C^0(\bar{\Omega})$ and $\chi_i|_e \in P_1(e)$ for all $e \in \mathcal{T}_h$ satisfying $\chi_i(\boldsymbol{a}_j) = \delta_{ij}$ for all $i, j = 1, ..., N$.

2.3 Numerical scheme

In order to formulate an implicit scheme for (2.1) we introduce the following forms for functions $\xi, \eta \in \mathcal{S}^h$:

$$\mathcal{M}(\xi, \eta)_h^n := \int_\Omega \Pi^h(\rho^n \xi \eta) dx, \tag{2.2}$$

$$\mathcal{A}(\xi, \eta)_h^n := \int_\Omega \Pi^h(\rho^n \xi) \Pi^h(\boldsymbol{v}^n) \cdot \nabla \eta dx, \tag{2.3}$$

$$\mathcal{D}(\xi, \eta)_h^n := \int_\Omega \mathcal{D}_c \Pi^h(\rho^n)\, \nabla \xi \cdot \nabla \eta dx, \tag{2.4}$$

$$\mathcal{F}(\eta)_h^n := \int_\Omega \Pi^h(\rho^n f^n \eta) dx. \tag{2.5}$$

We denote by U^n the approximation to $u(\cdot, t_n)$ and impose the discrete initial condition

$$U^0(\boldsymbol{a}_i) := \begin{cases} u^0(\boldsymbol{a}_i), & i \in \mathcal{N}_h^0, \\ 0, & \text{otherwise.} \end{cases} \tag{2.6}$$

Definition 2.4. (Scheme I) For each $n = 0, \dots, N_f - 1$ we seek a function $U^{n+1} \in \mathcal{S}^h$ such that $U^{n+1}(\boldsymbol{a}_i) = 0$ if $i \notin \mathcal{N}_h^{n+1}$ and satisfying

$$\delta_t \mathcal{M}(U^n, \eta)_h^n - \mathcal{A}(U^{n+1}, \eta)_h^{n+1} + \mathcal{D}(U^{n+1}, \eta)_h^{n+1} = \mathcal{F}_h^{n+1}(\eta) \quad \forall \eta \in \mathcal{S}^h. \tag{2.7}$$

Proposition 2.5. *The values $U^{n+1}(\boldsymbol{a}_i)$ for $i \in \mathcal{N}_h^{n+1}$ are determined from*

$$\frac{1}{\Delta t}\Big(\int_\Omega \{ (\Pi^h\big(\rho^{n+1} U^{n+1} \chi_j\big) - \Pi^h\big(\rho^n U^n \chi_j\big)\} dx \Big) - \int_\Omega \Pi^h\big(\rho^{n+1} U^{n+1}\big) \Pi^h(\boldsymbol{v}^{n+1}) \cdot \nabla \chi_j dx$$
$$+ \int_\Omega \mathcal{D}_c \Pi^h(\rho^{n+1})\, \nabla U^{n+1} \cdot \nabla \chi_j dx = \int_\Omega \Pi^h\big(\rho^{n+1} f^{n+1} \chi_j\big) dx \quad \textit{for all } j \in \mathcal{N}_h^{n+1} \tag{2.8}$$

whilst

$$U^{n+1}(\boldsymbol{a}_k) = 0, \ k \notin \mathcal{N}_h^{n+1}.$$

Proof. Equation (2.7) is equivalent to (2.8) for all $j \in \mathcal{N}$. First observe that if $j \notin \mathcal{N}_h^{n+1}$ then by definition ρ^{n+1} vanishes on the support of χ_j. Similarly if $j \notin \mathcal{N}_h^n$ then ρ^n vanishes on the support of χ_j. It remains to consider $j \in \mathcal{N}_h^n \setminus \mathcal{N}_h^{n+1}$. By the **discrete interface assumption** it follows that $\Pi^h(\rho^n U^n \chi_j) = 0$. This proves (2.8). By definition we impose that U^{n+1} vanishes on vertices lying outside $\mathcal{N}_h^{n+1}$. □

2.4 Unique solvability I

In order to show that the above system (2.8) indeed is solvable we will need the following estimate:

Lemma 2.6. *For $n = 1, \dots, N_f$, $\delta > 0$, and $\xi, \eta \in S_h$ we have that*

$$|\mathcal{A}(\xi, \eta)_h^n| \leq \delta \mathcal{D}(\eta, \eta)_h^n + \frac{||\boldsymbol{v}^n||_{\infty,\Omega}^2}{4\delta \mathcal{D}_c} \mathcal{M}(\xi, \xi)_h^n. \tag{2.9}$$

Proof. We infer the desired estimate from

$$|\mathcal{A}(\xi, \eta)_h^n| = \Big| \int_\Omega \Pi^h(\rho^n \xi) \Pi^h(\boldsymbol{v}^n) \cdot \nabla \eta dx \Big|$$
$$\leq \int_\Omega ||\boldsymbol{v}^n||_{\infty,\Omega} \Big| \sum_{i=1}^N \rho_i^n \xi_i \chi_i \Big| |\nabla \eta| dx \leq \sum_{i=1}^N \int_\Omega (\rho_i^n \chi_i)^{1/2} |\nabla \eta|\, ||\boldsymbol{v}^n||_{\infty,\Omega} (\rho_i^n \chi_i)^{1/2} |\xi_i| dx$$
$$\leq \sum_{i=1}^N \int_\Omega \Big(\mathcal{D}_c \delta \rho_i^n \chi_i |\nabla \eta|^2 + \frac{||\boldsymbol{v}^n||_{\infty,\Omega}^2}{4\delta \mathcal{D}_c} \rho_i^n \chi_i \xi_i^2 \Big) dx = \delta \mathcal{D}(\eta, \eta)_h^n + \frac{||\boldsymbol{v}^n||_{\infty,\Omega}^2}{4\delta \mathcal{D}_c} \mathcal{M}(\xi, \xi)_h^n$$

where we used the abbreviation $\rho_i^n = \rho(\boldsymbol{a}_i, t_n)$. □

Proposition 2.7. (Unique solvability) *If $\Delta t < 4\mathcal{D}_c / ||\boldsymbol{v}||_{\infty,\Omega_I}^2$ then* **Scheme I** *with the initial data* (2.6) *has a unique solution.*

Proof. Given a function $U^n \in \mathcal{S}^h$ such that $U^n(\boldsymbol{a}_k) = 0$ if $k \notin \mathcal{N}_h^n$ we have to show that the scheme yields a unique function $U^{n+1} \in \mathcal{S}^h$ with $U^{n+1}(\boldsymbol{a}_i) = 0$ if $i \notin \mathcal{N}_h^{n+1}$ and satisfying (2.7).
Taking W^{n+1} to be the difference of two possible solutions, it is sufficient to show that $W^{n+1} = 0$ is the only solution of

$$\mathcal{M}(W^{n+1}, \eta)_h^{n+1} - \Delta t \mathcal{A}(W^{n+1}, \eta)_h^{n+1} + \Delta t \mathcal{D}(W^{n+1}, \eta)_h^{n+1} = 0 \quad \forall \eta \in \mathcal{S}^h.$$

Taking $\eta = W^{n+1}$ and using (2.9) gives

$$(1 - \Delta t \frac{||\boldsymbol{v}^{n+1}||_{\infty,\Omega}^2}{4\delta \mathcal{D}_c}) \mathcal{M}(W^{n+1}, W^{n+1})_h^{n+1} + (1-\delta)\mathcal{D}(W^{n+1}, W^{n+1})_h^{n+1} \leq 0$$

which upon taking δ arbitrarily close to 1 yields for $\Delta t < 4\mathcal{D}_c / ||\boldsymbol{v}^{n+1}||_{\infty,\Omega}^2$,

$$\mathcal{M}(W^{n+1}, W^{n+1})_h^{n+1} = 0, \tag{2.10}$$
$$\mathcal{D}(W^{n+1}, W^{n+1})_h^{n+1} = 0. \tag{2.11}$$

It follows from (2.10) that $W^{n+1}(\boldsymbol{a}_i) = 0$ for all $i \in \mathcal{N}_{I,h}^{n+1}$. By (2.11) we have that $\nabla W^{n+1} = 0$ in every element $e \in \Gamma_h^{n+1}$, whence we conclude that also $W^{n+1}(\boldsymbol{a}_i) = 0$ for $i \in \mathcal{N}_{B,h}^{n+1}$. □

Recall that $\rho^{n+1}(\boldsymbol{a}_i) = 0$ for $i \in \mathcal{N}_{B,h}^{n+1}$ so that we cannot conclude directly from (2.10) that $W^{n+1} \equiv 0$ in the above proof.

Proposition 2.8. (Mass conservation) *If $f \equiv 0$ then it holds that for each $n \geq 1$*

$$\mathcal{M}(U^n, 1)_h^n = \mathcal{M}(U^0, 1)_h^0.$$

Proof. Taking $\eta = \sum_j \chi_j = 1$ in (2.7) yields in view of (2.8)

$$0 = \sum_{j \in \mathcal{N}_h^{n+1}} \int_\Omega \rho^{n+1}(\boldsymbol{a}_j) U^{n+1}(\boldsymbol{a}_j) \chi_j dx - \sum_{j \in \mathcal{N}_h^{n+1}} \int_\Omega \rho^n(\boldsymbol{a}_j) U^n(\boldsymbol{a}_j) \chi_j dx. \tag{2.12}$$

The first term is $\int_\Omega \Pi^h(\rho^{n+1}U^{n+1})dx = \mathcal{M}(U^{n+1}, 1)_h^{n+1}$. Concerning the second term, with the **discrete interface assumption** (Assumption 2.3) we have that $\rho^n(\boldsymbol{a}_j) = 0$ if $j \in \mathcal{N}_h^{n+1} \backslash \mathcal{N}_h^n$ so that we can replace the index set $\mathcal{N}_h^{n+1}$ in the sum by $\mathcal{N}_h^n$. Hence it gives $\int_\Omega \Pi^h(\rho^n U^n)dx = \mathcal{M}(U^n, 1)_h^n$ from which we infer the assertion. □

Remark 2.9. The above proposition can be extended to nontrivial source terms f. Total mass conservation is true for u subject to (1.1) provided that $\int_{\Gamma_0(t)} f(\cdot, t) = 0$ at all times $t \in I$. In the discrete setting this requirement on f naturally becomes $\sum_{i \in \mathcal{N}_h^n} \mathcal{F}(\chi_i)_h^n = 0$ for all n. We then see that (2.12) still holds true and we can conclude as before.

2.5 Edge smoothing

From the asymptotic analysis, Theorem 3.1 of [25], we expect an almost constant profile since a weighted L^2 norm of the derivative in the normal direction scales with ε. Formally, the equation (1.2) is closed with the boundary condition $(\rho u \boldsymbol{v} - \rho \mathcal{D}_c \nabla u) \cdot \boldsymbol{\nu} = 0$ on $\partial\Gamma_\varepsilon(t)$ where $\boldsymbol{\nu}$ is the external unit normal. In the continuous setting this condition is trivial because ρ vanishes on $\partial\Gamma_\varepsilon(t)$. However, in the discrete setting we are dealing with a nontrivial condition, since ρ is approximated there on a finite element grid.
This problem occurs already in the one-dimensional problem. Let $i \in \mathcal{N}_{B,h}^{n+1}$ be a boundary vertex such that $i-1 \in \mathcal{N}_{I,h}^{n+1}$. Inserting the basis function χ_i associated with the vertex i into (2.8) yields the equation for U_i^{n+1}. Since $\rho_i^{n+1} = \rho_{i+1}^{n+1} = 0$ it reads

$$
\begin{aligned}
-\frac{1}{\Delta t}\Big(\int_\Omega \chi_i dx\Big)\rho_i^n U_i^n - \Big(\int_\Omega \chi_{i-1}\Pi^h(\boldsymbol{v}^{n+1})\partial_x\chi_i dx\Big)\rho_{i-1}^{n+1}U_{i-1}^{n+1} \\
+ \Big(\int_\Omega \Pi^h(\rho^{n+1}dx)|\partial_x\chi_i|^2 dx\Big)U_i^{n+1} + \Big(\int_\Omega \Pi^h(\rho^{n+1})\partial_x\chi_{i-1}\partial_x\chi_i dx\Big)U_{i-1}^{n+1} = 0.
\end{aligned}
$$

Denoting by e the common support of χ_i and χ_{i-1}, let us write $\frac{h}{2}\tilde{\boldsymbol{v}}_{i-1,i}^{n+1} := \int_e \chi_{i-1}\Pi^h(\boldsymbol{v}^{n+1})$ and $\tilde{\rho}_{i-1,i}^{n+1} := \int_e \Pi^h(\rho^{n+1})$. We then obtain

$$
-\frac{h}{\Delta t}\rho_i^n U_i^n - \frac{1}{2}\tilde{\boldsymbol{v}}_{i-1,i}^{n+1}\rho_{i-1}^{n+1}U_{i-1}^{n+1} + \tilde{\rho}_{i-1,i}^{n+1}\frac{U_i^{n+1}-U_{i-1}^{n+1}}{h} = 0. \tag{2.13}
$$

Hence, in general U_i^{n+1} will be different from U_{i-1}^{n+1}. In numerical simulations we observed peaks associated with slopes enforced to U close to the boundary of the interfacial layer, cf. Figure 2.
In the case that ρ and $\nabla\rho$ vanish on $\partial\Gamma_\varepsilon(t)$ we may estimate the size of these peaks. We have that $\tilde{\rho}_{i-1,i}^{n+1} = \mathcal{O}(h^2)$ and $\rho_{i-1}^{n+1} = \mathcal{O}(h^2)$ as $h \to 0$, and we even have that $\rho_i^n = \mathcal{O}(\Delta t^2)$ as $\Delta t \to 0$. As a conclusion

$$
|U_i^{n+1} - U_{i-1}^{n+1}| = \mathcal{O}(h) \quad \text{as } h \to 0, \tag{2.14}
$$

and in Figure 2 we see that the height of the peaks indeed is linear in h.
Nevertheless, in some complex applications where the surface quantity enters other equations, perhaps in a phase field model for the surface evolution, one may desire profiles which are also flat at the edges to avoid edge effects. To achieve this goal we propose to add a kind of streamline diffusion term to **Scheme I** of the form

$$
\mathcal{L}(\xi,\eta)_h^{n+1} := \int_\Omega g_h^{n+1}\left(\boldsymbol{v}_{\boldsymbol{\nu},h}^{n+1}\cdot\nabla\xi\right)\left(\boldsymbol{v}_{\boldsymbol{\nu},h}^{n+1}\cdot\nabla\eta\right)dx \tag{2.15}
$$

for functions $\xi, \eta \in \mathcal{S}^h$. A normal velocity field $\boldsymbol{v}_{\boldsymbol{\nu}}(\boldsymbol{x},t)$ is obtained by projecting $\boldsymbol{v}(\boldsymbol{x},t)$ into a direction $\tilde{\boldsymbol{\nu}}(\boldsymbol{x},t)$, approximately normal to the boundary of $\Gamma_\varepsilon(t)$. How this field $\tilde{\boldsymbol{\nu}}$ is obtained depends on the application. For example, if the signed distance function to Γ is known one may choose $\tilde{\boldsymbol{\nu}} = \nabla d$. The approximation $\boldsymbol{v}_{\boldsymbol{\nu},h}$ to $\boldsymbol{v}_{\boldsymbol{\nu}}$ is constant on each element $e \in \mathcal{T}_h$ and coincides on e with the value of $\boldsymbol{v}_{\boldsymbol{\nu}}$ in the barycentre of e. The function g_h is constant on each element, too, and is of order h. It serves to add a small diffusion close to the boundaries of the interfacial layer. The above edge smoothing term furnishes an additional term of the form

$$
\tilde{g}_h^{n+1}|\tilde{\boldsymbol{v}}_{\boldsymbol{\nu},i-1,i}^{n+1}|^2\frac{U_i^{n+1}-U_{i-1}^{n+1}}{h}
$$

in (2.13). The values $\tilde{\rho}_{i-1,i}^{n+1}$ and ρ_{i-1}^{n+1} scale with h^2, and since g_h only scales with h this is a comparably large contribution resulting in

$$|U_i^{n+1} - U_{i-1}^{n+1}| = \mathcal{O}(h^2) \quad \text{as } h \to 0. \tag{2.16}$$

In the numerical experiments this procedure effectively smoothed out the profiles of U across the diffuse interfacial layer, see Figure 2.
Clearly, also the surface equation may be advection dominated in the sense that the tangential portion of the velocity is large compared with the (appropriately scaled) diffusivity. Streamline diffusion in the tangential direction then may be used to stabilise the problem. But we leave this discussion for future research and concentrate on diffusion dominated problems in this paper.

Definition 2.10. (Scheme II) For each $n = 0, \ldots, N_f - 1$ we seek a function $U^{n+1} \in \mathcal{S}^h$ such that $U^{n+1}(\boldsymbol{a}_k) = 0$ if $k \notin \mathcal{N}_h^{n+1}$ and satisfying

$$\delta_t \mathcal{M}(U^n, \eta)_h^n - \mathcal{A}(U^{n+1}, \eta)_h^{n+1} + \mathcal{D}(U^{n+1}, \eta)_h^{n+1} + \mathcal{L}(U^{n+1}, \eta)_h^{n+1} = 0 \quad \forall \eta \in \mathcal{S}^h. \tag{2.17}$$

2.6 Unique solvability II

Since (2.15) is a nonnegative term when $\xi = \eta$ the arguments used for proving Proposition 2.7 still can be applied. And thanks to the fact that only the gradient of η appears Proposition 2.8 is also true so that we may state:

Theorem 2.11. *If $\Delta t < 4\mathcal{D}_c / ||\boldsymbol{v}||_{\infty,\Omega_I}^2$ then* **Scheme II** *with the initial data* (2.6) *has a unique solution. Moreover, if $f \equiv 0$ then it holds that $\mathcal{M}(U^n, 1)_h^n = \mathcal{M}(U^0, 1)_h^0$ for all $n \in \{0, \ldots, N_f\}$.*

□

2.7 Discrete equations

Let k_n be the number of nodes in $\mathcal{N}_h^n$. We can decompose U^n as

$$U^n = \sum_{j \in \mathcal{N}_h^n} u_j^n \chi_j = \sum_{j \in \mathcal{N}_h^{n+1}} \tilde{u}_j^n \chi_j + \sum_{j \in \mathcal{N}_h^n \setminus \mathcal{N}_h^{n+1}} u_j^n \chi_j$$

where we note that

$$\tilde{u}_j^n := u_j^n \text{ for } j \in \mathcal{N}_h^{n+1} \cap \mathcal{N}_h^n \quad \text{and} \quad \tilde{u}_j^n := 0 \text{ for } j \in \mathcal{N}_h^{n+1} \setminus \mathcal{N}_h^n.$$

Let us furthermore write $\underline{u}^n := \{u_j^n\}_{j \in \mathcal{N}_h^{n+1}} \in \mathbb{R}^{k_n}$ and $\underline{\tilde{u}}^{n+1} := \{\tilde{u}_j^{n+1}\}_{j \in \mathcal{N}_h^{n+1}} \in \mathbb{R}^{k_{n+1}}$. We now define the matrices $M^{n+1}, K^{n+1}, L^{n+1}, \tilde{M}^n \in \mathbb{R}^{k_{n+1} \times k_{n+1}}$ with the entries

$$\begin{aligned}
M_{i,j}^{n+1} &:= \mathcal{M}(\chi_i, \chi_j)_h^{n+1}, \\
K_{i,j}^{n+1} &:= \mathcal{D}(\chi_i, \chi_j)_h^{n+1} - \mathcal{A}(\chi_i, \chi_j)_h^{n+1}, \\
L_{i,j}^{n+1} &:= \mathcal{L}(\chi_i, \chi_j)_h^{n+1}, \\
\tilde{M}_{i,j}^{n} &:= \mathcal{M}(\chi_i, \chi_j)_h^{n},
\end{aligned}$$

where the indices i, j belong to the set $\mathcal{N}_h^{n+1}$.

At each time step $n+1$ the solution U^{n+1} is obtained by solving the system

$$\left(\tfrac{1}{\Delta t}M^{n+1} + K^{n+1} + L^{n+1}\right)\underline{u}^{n+1} = \tfrac{1}{\Delta t}\tilde{M}^n\underline{\tilde{u}}^n \tag{2.18}$$

of k_{n+1} linear equations which have a unique solution, Proposition 2.7. These equations were solved using a stabilised BiCG method. Because ρ is zero at boundary points of $\mathcal{N}_h^{n+1}$ this system has some equations with small diagonal elements which leads to ill-conditioning. We remedy this by preconditioning using the inverse diagonal of $\frac{1}{\Delta t}M^{n+1} + K^{n+1} + L^{n+1}$.

2.8 Narrow band implementation

The numerical solution from time-step n to time-step $n+1$ involves $\Gamma_h^n \subset \mathcal{T}_h$ and $\Gamma_h^{n+1} \subset \mathcal{T}_h$. But these discrete interfaces do not differ very much. In fact, a time step restriction of the form $\Delta t \leq Ch/(||\boldsymbol{v}||_{\infty,\Omega_I})$ ensures not only that the **discrete interface assumption** is fulfilled but also that these sets differ at most by a single layer of elements. To take advantage of this in computations we define a narrow band of elements $\mathcal{B}_h^n \subset \mathcal{T}_h$ such that $\Gamma_h^n \cup \Gamma_h^{n+1} \subset \mathcal{B}_h^n$. This subset of elements is used to step from time level n to time level $n+1$. It does not necessarily change from time level to time level because of the accuracy requirement to resolve the movement of the surface as well as the solution of the surface equation. We take advantage of the fact that the other elements of $\mathcal{T}_h$ are not required in the calculation by dynamically adapting the triangulation. Each triangulation is a refinement of a coarse triangulation $\mathcal{T}_h^c$. Our assumption is that

Assumption 2.12. Narrow band assumption

- Each narrowband $\mathcal{B}_h^n$ can be obtained as a local refinement $\mathcal{T}_h^n$ of $\mathcal{T}_h^c$.
- Each narrowband $\mathcal{B}_h^n$ is a subset of $\mathcal{T}_h$.

At each time step we work on a triangulation $\mathcal{T}_h^n$ which is dynamically locally refined and coarsened whenever the narrow band changes by the removal or addition of layers of elements. As an example we show in Figure 1 two triangulations for the problem described in Subsection 3.2 involving an expanding circle.

Lemma 2.13. *If the* **narrow band assumption** 2.12 *is fulfilled then the values* $U^{n+1}(\boldsymbol{a}_i)$, $i \in \mathcal{N}_h^{n+1}$, *computed on* $\mathcal{T}_h^n$ *are the same as if they are computed on* $\mathcal{T}_h$, $n \in \{0, \ldots, N_f - 1\}$.

3 Numerical tests

In this section we describe experiments to test the accuracy of the numerical method for prescribed stationary and evolving surfaces for which a distance function is known. We here have situation (b) (as specified in the introduction) in mind and prescribe ρ by setting

$$\sigma(r) := \cos^2(r) \text{ if } |r| < \alpha_w := \tfrac{\pi}{2} \tag{3.1}$$

in (1.4) and by choosing the distance function to define r. The diffuse interfacial layer at time $t \in I$ then is $\Gamma(\varepsilon, t) = \left\{\boldsymbol{x} \in \Omega \,\middle|\, |d(\boldsymbol{x}, t)| \leq \alpha_w \varepsilon\right\}$ and has a thickness of $\pi\varepsilon$.

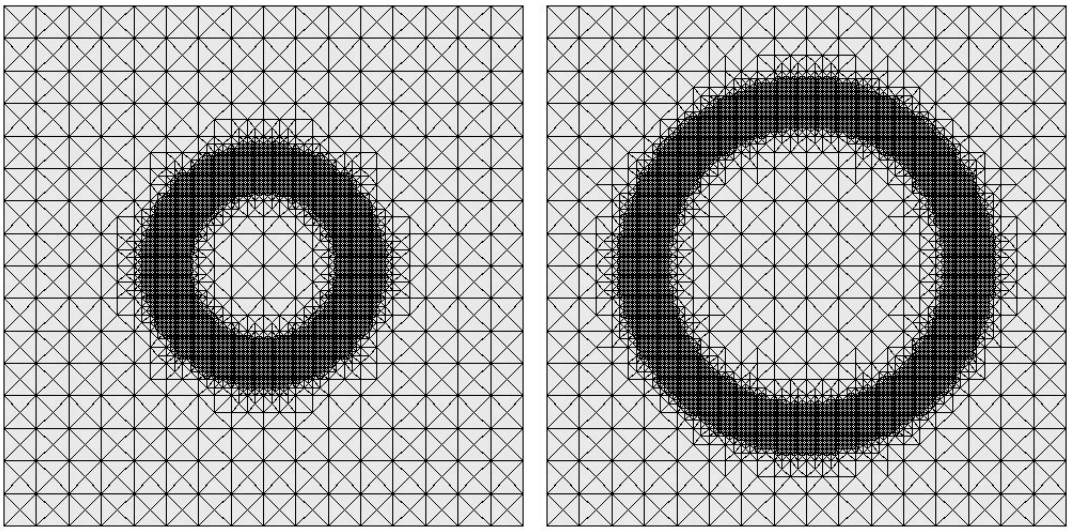

Figure 1: Triangulations at times $t = 0.0$ and $t = 0.1$ for the problem in Subsection 3.2 for the data $\varepsilon = 0.1$ and $h = 2^{-4.5}$.

h	$\frac{e[L^\infty,L^2]}{10^{-3}}$	eoc	$\frac{e[L^2,H^1]}{10^{-2}}$	eoc	$\frac{e[L^2,H^1_{\boldsymbol{\nu}_s}]}{10^{-2}}$	eoc	$\frac{e[L^2,H^1_{\boldsymbol{\tau}}]}{10^{-2}}$	eoc
$2^{-4.0}$	1.5628	—	1.8017	—	1.5629	—	0.8963	—
$2^{-4.5}$	1.5107	2.0167	1.5366	2.0538	1.3956	2.7323	0.6430	0.9098
$2^{-5.0}$	1.4848	3.2490	1.4065	2.0022	1.3307	2.2652	0.4582	0.9818
$2^{-5.5}$	1.4764	2.7846	1.3415	2.0268	1.3011	2.3742	0.3267	0.9290
$2^{-6.0}$	1.4723	—	1.3093	—	1.2881	—	0.2314	—

Table 1: Test problem on a moving circular interface described in Section 3.1, simulations without streamline diffusion term ($g_h \equiv 0$ in (2.15)). For a fixed value $\varepsilon \approx \sqrt{2}/10$ the errors measured for different mesh sizes are displayed. We also show the experimental orders of convergence obtained from the formula $eoc = \log|e(\sqrt{2}h) - e(h)|/|e(h) - e(h/\sqrt{2})|/\log\sqrt{2}$. We did not use the same formula as in Table 2 because the errors will not converge to zero as $h \to 0$ but to the error emerging from the approximation in ε.

Whenever edge smoothing is performed we use the function

$$g(\boldsymbol{x},t) := \begin{cases} 0 & \text{if } \frac{|d(\boldsymbol{x},t)|}{\varepsilon} \le \frac{\alpha_w}{2} \text{ or } \frac{|d(\boldsymbol{x},t)|}{\varepsilon} \ge \alpha_w, \\ h\frac{2}{\alpha_w}\big(\frac{|d(\boldsymbol{x},t)|}{\varepsilon} - \frac{\alpha_w}{2}\big) & \text{else} \end{cases} \tag{3.2}$$

and obtain g_h by evaluating g in the barycentres of the elements. In the subsequent tests, the diffusivity along the surface always was set to one, $\mathcal{D}_c = 1$.

ε	h	$\frac{e[L^\infty,L^2]}{10^{-3}}$	eoc	$\frac{e[L^2,H^1]}{10^{-2}}$	eoc	$\frac{e[L^2,H^1_{\boldsymbol{\nu}_s}]}{10^{-2}}$	eoc	$\frac{e[L^2,H^1_{\boldsymbol{\tau}}]}{10^{-2}}$	eoc
$\sqrt{2}/10$	$2^{-4.5}$	1.5107	—	1.5366	—	1.3956	—	0.6430	—
$1/10$	$2^{-5.0}$	0.7685	1.9502	0.9147	1.4967	0.7916	1.6361	0.4582	0.9777
$\sqrt{2}/20$	$2^{-5.5}$	0.3852	1.9929	0.5902	1.2642	0.4907	1.8010	0.3279	0.9654
$1/20$	$2^{-6.0}$	0.1930	1.9940	0.4272	0.9326	0.3587	0.9041	0.2319	0.9995

Table 2: Test problem on a moving circular interface described in Section 3.1, errors for simulations without streamline diffusion term ($g_h \equiv 0$ in (2.15)). For fixed ratio ε/h the errors and experimental orders of convergence (eoc) are shown. The latter ones are computed in the usual way via $\mathrm{eoc}(\varepsilon) = \log(\frac{e(\sqrt{2}\varepsilon)}{e(\varepsilon)})/\log(\sqrt{2})$ where e stands for the error under consideration.

3.1 Moving circle

We first present results on an example involving both advection along the surface and motion in the normal direction by prescribing Γ to be the circle of radius one in $\mathbb{R}^2$ moving at constant speed $\boldsymbol{v}_s = (2,0)^T$. Parametrising the circle in the form $\boldsymbol{\gamma}(s,t) = \boldsymbol{m}(t) + (\cos(s),\sin(s))^T$ where $\boldsymbol{m}(t) = (-0.5+2t,0)^T$ is its centre the function $u_0(\boldsymbol{\gamma}(s,t),t) := e^{-4t}\cos(s)\sin(s)$ is a solution to (1.1) with initial data $u_0(\boldsymbol{\gamma}(s,0),0) = \cos(s)\sin(s)$.
The distance function required for σ in (3.1), g or, respectively, g_h in (3.2) and the streamline diffusion term (2.15) is $d(\boldsymbol{x},t) = \|\boldsymbol{x}-\boldsymbol{m}(t)\| - 1$ and the (constant) velocity field was constantly extended to the simulation box $\Omega = [-2,2]^2$. The simulations were terminated at $t_f = 0.1$. For the triangulation $\mathcal{T}_h$ the domain Ω is split into four rectangular triangles $((-2,-2),(2,-2),(0,0))$, $((2,-2),(2,2),(0,0))$, $((2,2),(-2,2),(0,0))$, and $((-2,2),(-2,-2),(0,0))$ which are subsequently bisected until a desired maximal edge length h is achieved (we refer to [46] for the refinement procedure).
The simulation results presented below were obtained with the time step $\Delta t = h^2/20$. We observed that the approximation error due to the discretisation in time is negligible compared to the spatial discretisation error for Δt in this range.
To measure the error we computed the values

$$
\begin{aligned}
e[L^\infty,L^2](\varepsilon,h) &:= \max_{n=1,\dots,N_f}\Big(\sum_{l=0}^{L-1}\frac{2\pi}{L}\big|U^n(\boldsymbol{x}_l) - u(\boldsymbol{x}_l,t_n)\big|^2\Big)^{1/2},\\
e[L^2,H^1](\varepsilon,h) &:= \Big(\sum_{n=1}^{N_f}\Delta t\sum_{l=0}^{L-1}\frac{2\pi}{L}\big|\nabla U^n(\boldsymbol{x}_l) - \nabla_{\Gamma(t_n)}u(\boldsymbol{x}_l,t_n)\big|^2\Big)^{1/2},\\
e[L^2,H^1_{\boldsymbol{\nu}_s}](\varepsilon,h) &:= \Big(\sum_{n=1}^{N_f}\Delta t\sum_{l=0}^{L-1}\frac{2\pi}{L}\big|\nabla U^n(\boldsymbol{x}_l)\cdot\boldsymbol{\nu}_s(\boldsymbol{x}_l,t_n)\big|^2\Big)^{1/2},\\
e[L^2,H^1_{\boldsymbol{\tau}}](\varepsilon,h) &:= \Big(\sum_{n=1}^{N_f}\Delta t\sum_{l=0}^{L-1}\frac{2\pi}{L}\big|\nabla_{\Gamma(t_n)}U^n(\boldsymbol{x}_l) - \nabla_{\Gamma(t_n)}u(\boldsymbol{x}_l,t_n)\big|^2\Big)^{1/2},
\end{aligned}
\tag{3.3}
$$

where $\boldsymbol{x}_l := \boldsymbol{m}(t) + (\cos(s_l),\sin(s_l)^T$ with $s_l = 2\pi l/L$ for some $L \in \mathbb{N}$ (in practice, $L = 200$ turned out to be sufficient for that the error from the quadrature formula

was negligible compared to the discretisation errors). With respect to the H^1 norm we distinguish normal and tangential portions because we expect a different convergence behaviour. Clearly, the exact solution never involves a derivative in the normal direction $\boldsymbol{\nu}_s$ so that $e[L^2, H^1_{\boldsymbol{\nu}_s}]$ measures an error of the finite element approximation only.
Table 1 displays errors and convergence orders for the simulations without the edge smoothing term and for ε fixed. The experimental orders of convergence are obtained from the formula $eoc = \log|e(\sqrt{2}h) - e(h)|/|e(h) - e(h/\sqrt{2})|/\log\sqrt{2}$. We used this formula because the errors will not converge to zero as $h \to 0$ but to the error emerging from the approximation in ε. We observe (at least) quadratic convergence of $e[L^\infty, L^2]$ and of $e[L^2, H^1_{\boldsymbol{\nu}_s}]$ and linear convergence of $e[L^2, H^1_{\boldsymbol{\tau}}]$ as $h \to 0$. That also $e[L^2, H^1]$ seems to converge much better than linear lies in the fact that the error is dominated by its normal portion but one will expect that for small h the tangential portion dominates because of its linear convergence.
Taking the streamline diffusion term into account by defining g_h as in (3.2) has almost no impact on the size of the errors indicating that the approximation U is only affected close to the boundary of the interfacial layer $\Gamma(\varepsilon)$ but not in its centre on Γ.
Keeping the ratio ε/h or, equivalently, the number of grid points K across the interface fixed we observe a surprisingly good convergence behaviour as $\varepsilon \to 0$, namely quadratic of $e[L^\infty, L^2]$ and linear of $e[L^2, H^1_{\boldsymbol{\tau}}]$ (see Table 2). The asymptotic analysis in [25] suggests quadratic convergence of $e[L^2, H^1_{\boldsymbol{\nu}_s}]$. We observed that the larger is the number K of points across the interfacial layer the better is the experimental order of convergence in ε of $e[L^2, H^1_{\boldsymbol{\nu}_s}]$.

3.2 Expanding circle

In this test example we consider an expanding circle centred in 0 and radius $r(t) = 0.75+5t$. The velocity field is given by $\boldsymbol{v}_s(\boldsymbol{x}, t) = 5\boldsymbol{x}/|\boldsymbol{x}|$ and, hence, purely in the normal direction. The function $u_s(\boldsymbol{x}, t) := \exp(\frac{4}{5r(t)})\frac{x_1 x_2}{r(t)|\boldsymbol{x}|^2}$ is a solution to (1.1). To see this one may again parameterise the moving circle in the form $\boldsymbol{\gamma}(s, t) = r(t)(\cos(s), \sin(s))^T$, $t \in [0, \infty)$, $s \in (0, 2\pi)$ and then conclude using that $\nabla_\Gamma = (-\sin(s), \cos(s))^T \frac{1}{|\boldsymbol{\gamma}(t,s)|}\partial_s$.
The above formula for $\boldsymbol{v}_s$ has been extended to the interfacial layer for defining $\boldsymbol{v}$ and the distance function is given by $d(\boldsymbol{x}, t) = \|\boldsymbol{x}\|_2 - r(t)$. The triangulation $\mathcal{T}_h$ was obtained as in the preceeding section, and the time step $\Delta t = h^2/20$ was small enough again so that approximation errors due to the time discretisation are negligible.
Figure 2 displays concentration profiles across the interface at time $t = 0.5$ at the point $\boldsymbol{x} = (\cos(\frac{3}{8}\pi), \sin(\frac{3}{8}\pi))$. As predicted in Section 2.5, the computation without edge smoothing involves layers close to the boundary of the diffuse interface. We observe a peak in the direction of the motion, i.e., to the right, and the other way around to the left. Recall that U is set to zero in grid points not belonging to $\mathcal{N}_h$ which explains the sharp drops at the boundary of the layer. As the grid is refined the peaks become less pronounced, and from the figure we see that their height is proportional to h. This is in agreement with the analysis in Section 2.5, see Equation (2.14). The edge smoothing term, added by computing g_h from (3.2), makes these boundary layers much smaller as desired.
We evaluated the errors (3.3) choosing the quadrature points $\boldsymbol{x}_l = r(t_n)(\cos(s_l), \sin(s_l))$, $s_l = 2\pi l/L$ at time t_n (again, $L = 200$ turned out to yield a sufficient accuracy). As in the previous example in Section 3.1, $e[L^\infty, L^2]$ converges quadratically and $e[H^1_{\boldsymbol{\tau}}]$ linearly as $\varepsilon \to 0$ whilst keeping the ratio ε/h constant. Furthermore, as in the previous

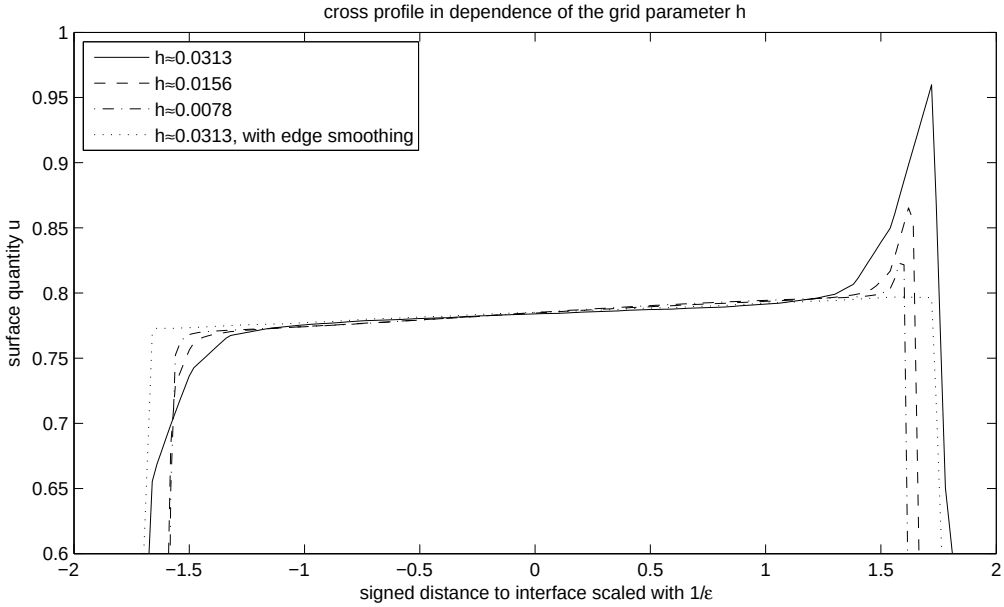

Figure 2: Test problem on an expanding circle. The profiles of the computed solution U across the interfacial layer are displayed for several values of h and fixed $\varepsilon = \sqrt{2}/10$. For comparison, a profile computed with edge smoothing is displayed. Outside the interfacial layer the value of U has always been set to 0 which explains the sharp drops of the profiles on the left and right.

example the errors with edge diffusion quantitatively almost are the same as the errors without.

The dependence of the cross section profiles with edge smoothing on the thickness parameter ε is shown in Figure 3 (time $t = 0.5$ and point $\boldsymbol{x} = (\cos(\frac{3}{8}\pi), \sin(\frac{3}{8}\pi))$ again). The figure reveals that the profile becomes flatter as the interface thickness becomes smaller (in comparison with Figure 2 the reader should be aware of the different scalings of the y-axes; in fact, the dashed line in Figure 3 corresponds to the dotted line in Figure 2). Yet there are still some minor boundary layers that affect, in particular, the slope of the profile in the interface centre, i.e., the gradient of U in the normal direction on Γ. The error $e[L^2, H^1_{\boldsymbol{\nu}_s}]$ measuring this effect decays if the number of grid points across the diffuse interface is increased.

3.3 3D example

In order to test the method in three space dimensions we consider Example 7.3 from [19] concerning an oscillating ellipsoid of the form

$$\Gamma(t) := \left\{ \boldsymbol{x} = (x_1, x_2, x_3)^T \in \mathbb{R}^3 \;\middle|\; \frac{x_1^2}{a(t)} + x_2^2 + x_3^2 = 1 \right\}$$

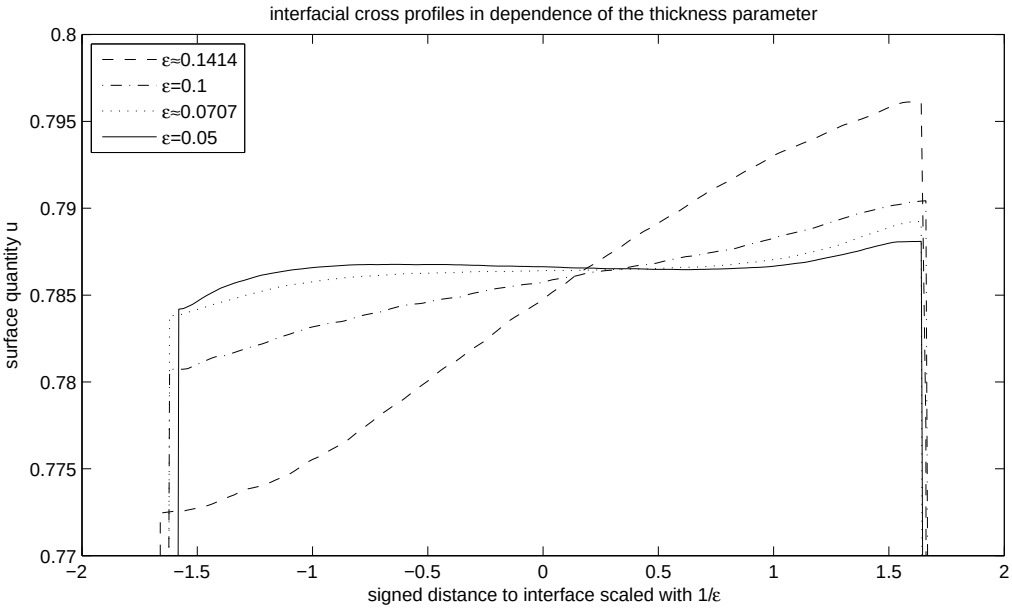

Figure 3: Test problem on an expanding circle. The profiles of the computed function U across the interfacial layer are displayed for several values of ε, keeping the ratio ε/h constant (we ensured at least $K = 16$ grid points across the interface). The distance is to the limiting interface Γ is scaled with $1/\varepsilon$ which allows a better comparison of the profiles for different values of ε. In comparison with Figure 2 the reader should be aware of the different scalings of the x and y axes.

where $a(t) := 1 + \sin(t)/4$. As associated velocity field we choose

$$\boldsymbol{v}_s(\boldsymbol{x}, t) := \frac{\partial_t a(t)}{a(t)} \begin{pmatrix} x_1 \\ 0 \\ 0 \end{pmatrix}$$

obtained from prescribing the trajectories of mass points on the initial surface to be $\boldsymbol{x}(t) := (\sqrt{a(t)}x_1(0), x_2(0), x_3(0))^T$ with $\boldsymbol{x}(0) \in \Gamma(0)$. Thus both advection along the surface and deformation by motion in the normal direction is involved.
On the stationary two-dimensional unit sphere S^2 the function $u_s(\boldsymbol{x}, t) := e^{-6t}x_1x_2$ is a solution to the surface heat equation $\partial_t u_s - \Delta_{S^2} u_s = 0$. Setting $\mathcal{D}_c = 1$, the function u_s also is a solution to (1.1) for the above data $(\Gamma, \boldsymbol{v}_s)$ provided that

$$f_s(\boldsymbol{x}, t) := u_s(\boldsymbol{x}, t)\Big\{ -6 + \frac{\partial_t a(t)}{a(t)}\Big(1 - \frac{x_1^2}{2N}\Big) + \frac{1 + 5a(t) + 2a(t)^2}{N} \\ - \frac{1 + a(t)}{N^2}\Big(x_1^2 + a(t)^3(x_2^2 + x_3^2)\Big)\Big\}$$

where $N := x_1^2 + a(t)^2(x_2^2 + x_3^2)$.
For the simulations, the velocity field $\boldsymbol{v}_s$ and the right hand side f_s have been extended constantly in the normal direction away from Γ in order to define $\boldsymbol{v}$ and f, respectively.

The computational domain was $\Omega = [-2,2]^3$ and the final time $t_f = 4$. The triangulation $\mathcal{T}_h$ was obtained by starting with six tetrahedra with vertices coinciding with the corners of Ω and subsequent refinement by bisection (see [46] for the algorithms) until the desired maximal edge length h was achieved. The results are presented for the time step $\Delta t = h^2/2.0$. Edge smoothing with g_h computed from (3.2) has been taken into account.
To measure the error we have to integrate functions defined on the ellipsoids $\Gamma(t_n)$. Parameterising in the form

$$\boldsymbol{x}(\phi,\theta) = \begin{pmatrix} \sqrt{a(t)}\cos(\phi)\sin(\theta) \\ \sin(\phi)\sin(\theta) \\ \cos(\theta) \end{pmatrix}, \quad (\phi,\theta) \in [0,2\pi) \times [0,\pi]$$

we applied the following integration formula (for a function F on $\Gamma(t_n)$):

$$\begin{aligned} \int_{\Gamma(t_n)} F(\boldsymbol{x}) d\mathcal{H}^2 &= \int_0^{\pi} \int_0^{2\pi} F(\boldsymbol{x}(\phi,\theta)) \sqrt{g_{a(t_n)}(\phi,\theta)}\, d\phi d\theta \\ &\approx \sum_{k=1}^{L-1} \sum_{j=0}^{2L-1} F(\boldsymbol{x}(\phi_j,\theta_k)) \sqrt{g_{a(t_n)}(\phi_j,\theta_k)}\, \delta^2 =: I_n[F] \end{aligned}$$

where

$$g_{a(t)}(\phi,\theta) = a(t)\sin(\theta)^2\big(\cos(\theta)^2 + \sin(\phi)^2\sin(\theta)^2\big) + \cos(\phi)^2\sin(\theta)^4$$

and $\phi_j = j\delta$, $\theta_k = k\delta$ with $\delta = \pi/L$. In practice, $L = 400$ turned out to yield sufficiently accurate values. To measure the error we computed the values

$$\begin{aligned} e[L^\infty, L^2](\varepsilon,h) &:= \max_{n=1,\dots,N_f} \sqrt{I_n\big[|U^n(\cdot) - u(\cdot,t_n)|^2\big]}, \\ e[L^2, H^1_{\boldsymbol{\nu}_s}](\varepsilon,h) &:= \Big(\sum_{n=1}^{N_f} \Delta t I_n\big[|\nabla U^n(\cdot)\cdot\boldsymbol{\nu}_s(\cdot,t_n)|^2\big]\Big)^{1/2}, \\ e[L^2, H^1_{\boldsymbol{\tau}}](\varepsilon,h) &:= \Big(\sum_{n=1}^{N_f} \Delta t I_n\big[|\nabla_{\Gamma(t_n)} U^n(\cdot) - \nabla_{\Gamma(t_n)} u(\cdot,t_n)|^2\big]\Big)^{1/2}. \end{aligned}$$

Tables 3, 4, and 5 display the errors for grids (h fixed in each row) and several interfacial thicknesses (ε fixed in each column). The values support the convergence rates in h and in ε as obtained in the two-dimensional case. We remark that the influence of the time step is not negligible in the chosen range (recall that here $\Delta t = h^2/2$ whilst in the previous two-dimensional examples we had $\Delta t = h^2/20$). Simulations for different time steps at fixed ε and h reveal linear convergence as one would expect since a backward Euler time stepping procedure is applied.

4 Phase field surfaces

In this section we describe how the proposed method may be applied to diffuse interfaces arising from computation of phase field equations. Typically in applications the

$e[L^\infty, L^2](\varepsilon, h)/10^{-2}$					
$h \setminus \varepsilon$	$2/10$	$\sqrt{2}/10$	$1/10$	$\sqrt{2}/20$	$1/20$
≈ 0.1088	1.6019				
≈ 0.0628	0.9062	0.6621			
≈ 0.0544	0.7633	0.5148	0.4056		
≈ 0.0314	0.5879	0.3372	0.2224	0.1716	
≈ 0.0272	0.5536	0.3029	0.1849	0.1287	0.1047

Table 3: Data for an advection-diffusion equation with source term on an oscillating ellipsoid in 3D described in Section 3.3.

$e[L^2, H^1_{\boldsymbol{\nu}_s}](\varepsilon, h)/10^{-2}$					
$h \setminus \varepsilon$	$2/10$	$\sqrt{2}/10$	$1/10$	$\sqrt{2}/20$	$1/20$
≈ 0.1088	5.2990				
≈ 0.0628	4.7355	3.0320			
≈ 0.0544	4.4975	2.7484	1.9132		
≈ 0.0314	4.2993	2.4456	1.5070	1.1016	
≈ 0.0272	4.2333	2.3526	1.3828	0.9499	0.7901

Table 4: Data for an advection-diffusion equation with source term on an oscillating ellipsoid in 3D described in Section 3.3.

evolution of the surface will be linked to the solution of the equation on the surface and possibly also to equations holding in a bulk domain, [35, 23]. The purpose of the numerical examples in this section is to indicate how our approach may be used in the context of the surface being computed by a phase field method.

4.1 Diffusion on a geometrically evolving interface

In these examples the evolution of the surface does not depend on the solution of the surface equation.

4.1.1 Allen Cahn variational inequality

We consider the diffusion of a scalar function u on a surface $\Gamma(t)$ that is evolving with a velocity $\boldsymbol{v} = V\boldsymbol{\nu}_s$ given by the curvature dependent flows

$$V = -H + p, \tag{4.1}$$

$$V = -H + \frac{1}{|\Gamma|}\int_\Gamma H, \tag{4.2}$$

$e[L^2, H^1_\tau](\varepsilon, h)/10^{-2}$					
$h \setminus \varepsilon$	$2/10$	$\sqrt{2}/10$	$1/10$	$\sqrt{2}/20$	$1/20$
≈ 0.1088	5.0222				
≈ 0.0628	3.4891	3.4363			
≈ 0.0544	2.6220	2.5583	2.5417		
≈ 0.0314	1.8222	1.7362	1.7187	1.7103	
≈ 0.0272	1.4208	1.3021	1.2768	1.2695	1.2632

Table 5: Data for an advection-diffusion equation with source term on an oscillating ellipsoid in 3D described in Section 3.3.

where H denotes the mean curvature of the surface $\Gamma(t)$. Equation (4.1) is forced mean curvature flow with a prescribed forcing p whereas (4.2) is volume conserving mean curvature flow in which the volume bounded by $\Gamma(t)$ is constant. We set the velocity $\boldsymbol{v}_s = V\boldsymbol{\nu}_s$ in (1.1) and do not consider advection on the surface.
The evolving surface is approximated by an evolving diffuse interface $\Gamma_\varepsilon(t)$ given by the zero level set of a phase field variable $\varphi(\cdot, t)$. Following Blowey and Elliott, we employ a double-well potential of double obstacle type

$$W(r) = \begin{cases} \frac{1}{2}(1 - r^2) & \text{if } |r| \le 1, \\ \infty & \text{else,} \end{cases} \tag{4.3}$$

[9, 11, 14].
The appropriate space for φ is

$$\varphi(\cdot, t) \in \mathcal{K} := \{\eta \in H^1(\Omega) : \ |\eta| \le 1 \text{ a.e. } \Omega\}.$$

This yields the following Allen-Cahn variational inequality:
($\mathbf{P}$) Find $\varphi \in \mathcal{K}$ such that

$$\int_\Omega \big(\varepsilon\varphi_t(\eta - \varphi) + \varepsilon\nabla\varphi \cdot (\nabla\eta - \nabla\varphi) - \tfrac{\varphi}{\varepsilon}(\eta - \varphi) - C_W p(\eta - \varphi)\big)dx \ge 0 \ \forall \eta \in \mathcal{K} \tag{4.4}$$

$$\varphi(\cdot, 0) = \varphi_0(\cdot). \tag{4.5}$$

Combining ($\mathbf{P}$) with the volume constraint $\frac{1}{|\Omega|}\int_\Omega \varphi = \mathcal{M}$ for a given $\mathcal{M} \in (-1, 1)$ we obtain the volume conserving Allen-Cahn type problem:
($\mathbf{P}_\mathcal{M}$) Find $\varphi \in \mathcal{K}_\mathcal{M} := \{\eta \in \mathcal{K} | \ \frac{1}{|\Omega|}\int_\Omega \eta = \mathcal{M}\}$ and Lagrange multiplier $\lambda(t)$ such that

$$\int_\Omega \big(\varepsilon\varphi_t(\eta - \varphi) + \varepsilon\nabla\varphi \cdot (\nabla\eta - \nabla\varphi) - \tfrac{\varphi}{\varepsilon}(\eta - \varphi)\big)dx \ge \int_\Omega \lambda(\eta - \varphi)dx \ \forall \eta \in \mathcal{K} \tag{4.6}$$

$$\varphi(\cdot, 0) = \varphi_0(\cdot). \tag{4.7}$$

We consider the situation where $\Gamma(t)$ evolves smoothly with no change in topology and set $d(\cdot, t)$ to be the signed distance function to $\Gamma(t)$. The initial condition is taken to be

$$\varphi_0(\cdot) = \psi(\frac{d(\cdot, 0)}{\varepsilon}). \tag{4.8}$$

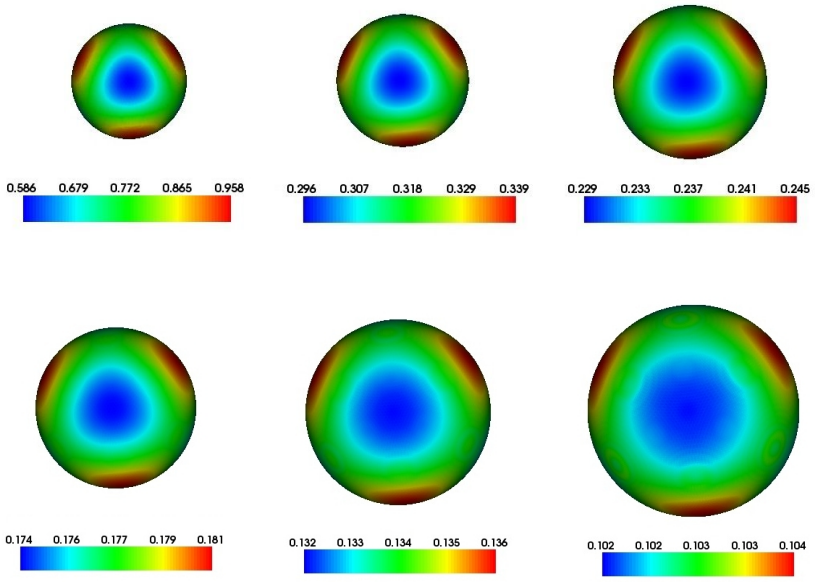

Figure 4: Diffusion on a surface evolving with forced mean curvature flow

An asymptotic analysis (cf. [11]) with $C_W = \frac{\pi}{4}$ yields that the transition profile of the phase variable is given by

$$\psi(r) = \begin{cases} -1 & \text{if } r \leq -\frac{\pi}{2}, \\ \sin(r) & \text{if } |r| < \frac{\pi}{2}, \\ 1 & \text{if } r \geq \frac{\pi}{2}, \end{cases} \tag{4.9}$$

and for small ε, solutions to $(\mathbf{P})$ and $(\mathbf{P}_{\mathcal{M}})$ are of the form

$$\varphi(\boldsymbol{x}, t) = \psi(d(\boldsymbol{x}, t)/\varepsilon)) + O(\varepsilon) \quad \boldsymbol{x} \in \{|\varphi(\cdot, t)| < 1\} \tag{4.10}$$

where $d(x, t)$ is the signed distance function to an evolving hypersurface, see [11]. The zero level set of φ is an approximation to this hypersurface with an error $O(\varepsilon^2)$ in the Hausdorff distance, [14, 40, 15].
The phase field equations are discretised using the finite element method described earlier. In particular we employed the time discrete approximations

$$\begin{aligned} \int_\Omega \left(\varepsilon \delta_t \varphi_h^n (\eta - \varphi_h^{n+1}) + \varepsilon \nabla \varphi_h^{n+1} \cdot (\nabla \eta - \nabla \varphi_h^{n+1}) - \tfrac{1}{\varepsilon} \varphi_h^{n+1} (\eta - \varphi_h^{n+1})\right) dx \\ \geq \int_\Omega p^n (\eta - \varphi_h^{n+1}) dx \ \forall \eta \in \mathcal{K}^h \end{aligned} \tag{4.11}$$

$$\varphi_h(\cdot, 0) = \varphi_{h,0}(\cdot). \tag{4.12}$$

Here $p^n = C_W g(\cdot, t^{n+1})$ and $\varphi_h^{n+1} \in \mathcal{K}^h$ to define $(\boldsymbol{P}^h)$ or $p^n = \lambda^{n+1} \in \mathbb{R}$ (which needs to be computed in order to impose the mean value constraint on φ_h^{n+1}) and $\varphi_h^{n+1} \in \mathcal{K}^h_{\mathcal{M}}$ to define $(\boldsymbol{P}^h_{\mathcal{M}})$ with

$$\mathcal{K}^h = \{\eta \in \mathcal{S}^h : \ |\eta| \leq 1\}, \quad \mathcal{K}^h_{\mathcal{M}} = \{\eta \in \mathcal{K}^h : \ \frac{1}{|\Omega|} \int_\Omega \eta = \mathcal{M}\}.$$

4.1.2 Coupling to the diffuse surface equation

The phase field models provide the data for the surface to be used in (1.2) in the following way. In the continuous problem the diffuse interfacial layer is defined by $|\varphi| < 1$ and we set

$$\rho := 1 - \varphi^2 \tag{4.13}$$

and define a diffuse interface velocity field by

$$\boldsymbol{v} := \frac{\varphi_t}{|\nabla\varphi|}\boldsymbol{\nu} \tag{4.14}$$

where $\boldsymbol{\nu} := \frac{\nabla\varphi}{|\nabla\varphi|}$ is the normal to the level sets of φ.
In (2.17) we then use the solution of the double obstacle problem by setting

$$\rho^n := 1 - (\varphi_h^n)^2$$

and replace $\Pi^h(\boldsymbol{v}^n)$ by a computed discrete diffuse interface velocity given by

$$\boldsymbol{v_h^n} := \frac{\delta_t\varphi_h^n}{|\nabla\varphi_h^n|}\boldsymbol{\nu}_h^n, \quad \boldsymbol{\nu}_h^n := \frac{\nabla\varphi_h^n}{|\nabla\varphi_h^n|}.$$

Note that on an element in the computational interface φ_h^n will not be identically 1 or -1 and $|\nabla\varphi_h^n|$ does not vanish.

4.1.3 Narrow band implementation

The interfacial region has a thickness that is proportional to ε and so in order to resolve this interfacial layer it is necessary to choose $h \ll \varepsilon$. However the solution of a discrete double obstacle phase field problem is only required in a narrow band consisting of the elements in which $|\varphi_h^{n-1}| < 1$ and neighbouring elements. This can be taken advantage of in several ways, (see [15, 28] for details). In particular away from the interfacial layer of elements in the bulk domain the mesh size h can be chosen larger since the solution is known there. A guard layer of elements is maintained around the interfacial region. The mesh is dynamically locally refined and coarsened in order to maintain the **Narrow band assumption** 2.12, see [28, 6]. This *Sharp diffuse interface front tracking approach* automatically yields the sets $\mathcal{B}_h^n$ and Γ_h^n to be used for solving the surface partial differential equation.
The discrete variational inequalities ($\mathbf{P^h}$) and ($\mathbf{P^h_{\mathcal{M}}}$) were solved using the semi-smooth Newton algorithms presented in [8]. Alternative methods are projected successive over relaxation or the direct multi-grid approach, [30].

4.1.4 Computations

Example 4.1. Convergence study In this test example we consider the expanding circular interface problem defined in Section 3.2. In particular we set $p = 5 + \frac{1}{0.75-5t}$ in (4.4) and took $\Omega = [-1.1, 1.1]^2$, $\Delta t = h^2$, $L = 200$ and $N_f\Delta t = 0.05$. The errors $e[L^\infty, L^2]$ and $e[L^2, H^1]$ are shown in Tables 6, 7, 8, 9, and 10 where we see, as in Section 3.2, that the error $e[L^\infty, L^2]$ converges quadratically and the error $e[L^2, H^1]$ converges linearly for resolved ε computations.

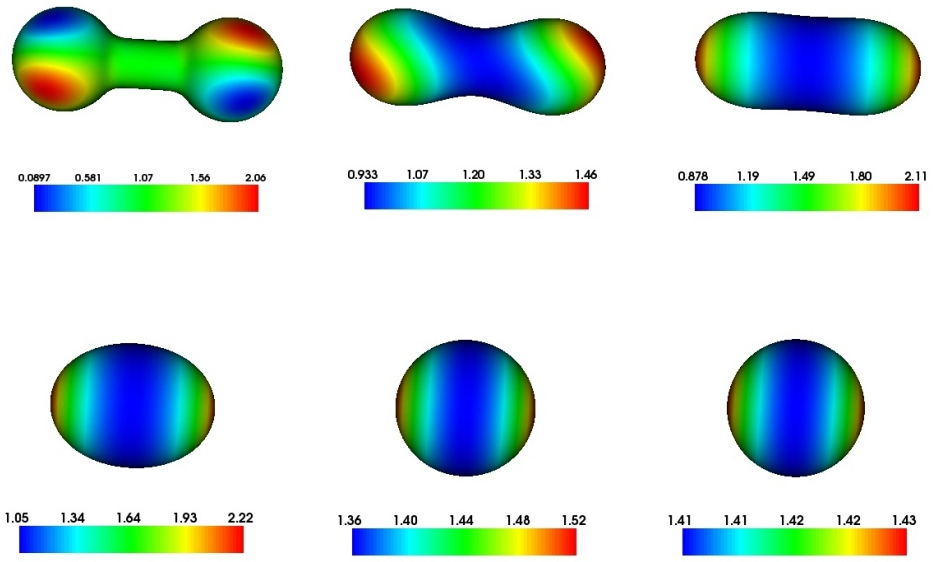

Figure 5: Diffusion on a surface evolving with conserved mean curvature flow

ε	h	$\frac{e[L^\infty,L^2]}{10^{-2}}$	$\frac{e[L^2,H^1]}{10^{-1}}$	$\frac{e[L^2,H^1_{\nu_s}]}{10^{-1}}$	$\frac{e[L^2,H^1_\tau]}{10^{-2}}$
$\pi/6$	$\approx 5.288 \cdot 10^{-3}$	4.5102	0.9706	0.9506	1.9614
$\pi/9$	$\approx 3.525 \cdot 10^{-3}$	1.9368	0.6490	0.6428	0.8925
$\pi/12$	$\approx 2.644 \cdot 10^{-3}$	0.9848	0.4883	0.4855	0.5241
$\pi/18$	$\approx 1.763 \cdot 10^{-3}$	0.3366	0.3287	0.3259	0.4337

Table 6: Errors for simulations without streamline diffusion term ($g_h \equiv 0$ in (2.15)) for the expanding circular interface described in Example 4.1.

Example 4.2. Forced mean curvature flow in 3D This is an example of diffusion on an expanding sphere evolving by forced mean curvature flow. In Figure 4 we consider the domain $\Omega = [-1,1]^3 \subset \mathbb{R}^3$ and set $\varepsilon = \frac{1}{8\pi}$. In the initial thin diffuse interface we set

$$u(\boldsymbol{x},0) = 1 + 20x_1x_2x_3.$$

Furthermore we set the diffusion coefficient to be $\mathcal{D}_c = 1$ and the forcing function in (4.4) to be $p = 6$. We had a minimal edge length of $h_{\min} = 2^{-7} \approx 0.00781$ in the narrow bands $\mathcal{B}_h^n$ while $h_{\max} = 2^{-2.5} \approx 0.177$ in the bulk. The timestep $\Delta t = 5 \cdot 10^{-5}$. The six subplots in Figure 4 display the scalar function U^n on the zero isosurfaces of φ_h^n at times $t = 0, 0.02, 0.04, 0.06, 0.08$ and 0.1.

Example 4.3. Volume conserved mean curvature flow in 3D This is an example of diffusion on a surface evolving by mean curvature flow forced so that the volume inside the surface is conserved, which in the long term leads to a stationary sphere. In

$e[L^\infty, L^2](\varepsilon, h)/10^{-2}$				
$h \setminus \varepsilon$	$\pi/6$	$\pi/9$	$\pi/12$	$\pi/18$
$\approx 5.288 \cdot 10^{-3}$	4.5102			
$\approx 3.525 \cdot 10^{-3}$	4.5896	1.9368		
$\approx 2.644 \cdot 10^{-3}$	4.6192	1.9995	0.9848	
$\approx 1.763 \cdot 10^{-3}$	4.6472	2.0642	1.0978	0.3366

Table 7: Data for the expanding circular interface described in Example 4.1

$e[L^2, H^1](\varepsilon, h)/10^{-1}$				
$h \setminus \varepsilon$	$\pi/6$	$\pi/9$	$\pi/12$	$\pi/18$
$\approx 5.288 \cdot 10^{-3}$	0.9706			
$\approx 3.525 \cdot 10^{-3}$	0.9848	0.6490		
$\approx 2.644 \cdot 10^{-3}$	0.9888	0.6547	0.4883	
$\approx 1.763 \cdot 10^{-3}$	0.9918	0.6598	0.4929	0.3287

Table 8: Data for the expanding circular interface described in Example 4.1

Figure 5 we consider the domain $\Omega = [-1.2, 1.2] \times [-1, -1] \times [-1, 1] \subset \mathbb{R}^3$, the diffusion coefficient is $\mathcal{D}_c = 0.1$, $\varepsilon = \frac{1}{8\pi}$, and

$$u(\boldsymbol{x}, 0) = 1 + 20x_1x_2x_3.$$

We again had a minimal edge length of $h_{\min} = 2^{-7} \approx 0.00781$ in the narrow bands $\mathcal{B}_h^n$ while $h_{\max} = 2^{-2.5} \approx 0.177$ in the bulk. The timestep $\Delta t = 5 \cdot 10^{-5}$. The six subplots in Figure 5 display the scalar function U^n on the zero isosurfaces of φ_h^n at times $t = 0, 0.05, 0.1, 0.2, 0.35$ and 0.5.

4.2 Diffusion on an interface in two-phase flow

In this second application example our aim is to compute the advection and diffusion of an insoluble surfactant on the interface between two immiscible fluids. The model for the two-phase flow consists of an incompressible Navier-Stokes system coupled to an advective Cahn-Hilliard equation derived in [12] but we consider a double-well potential of obstacle type as (4.3), [11], and assume equal mass densities and viscosities in both fluid phases. In dimensionless and weak form, the Navier-Stokes system consisting of

$e[L^2, H^1_{\boldsymbol{\tau}}](\varepsilon, h)/10^{-2}$				
$h \setminus \varepsilon$	$\pi/6$	$\pi/9$	$\pi/12$	$\pi/18$
$\approx 5.288 \cdot 10^{-3}$	1.9614			
$\approx 3.525 \cdot 10^{-3}$	1.9394	0.8925		
$\approx 2.644 \cdot 10^{-3}$	1.9359	0.8682	0.5241	
$\approx 1.763 \cdot 10^{-3}$	1.9335	0.8614	0.4840	0.4337

Table 9: Data for the expanding circular interface described in Example 4.1

$e[L^2, H^1_{\boldsymbol{\nu}_s}](\varepsilon, h)/10^{-1}$				
$h \setminus \varepsilon$	$\pi/6$	$\pi/9$	$\pi/12$	$\pi/18$
$\approx 5.288 \cdot 10^{-3}$	0.9506			
$\approx 3.525 \cdot 10^{-3}$	0.9655	0.6428		
$\approx 2.644 \cdot 10^{-3}$	0.9697	0.6489	0.4855	
$\approx 1.763 \cdot 10^{-3}$	0.9728	0.6542	0.4905	0.3259

Table 10: Data for the expanding circular interface described in Example 4.1

mass and momentum balance reads

$$0 = \int_\Omega \zeta \nabla \cdot \boldsymbol{v} dx, \ \forall \zeta \in L^2(\Omega), \tag{4.15}$$

$$\begin{aligned} 0 = &\int_\Omega \big(\partial_t \boldsymbol{v} \cdot \boldsymbol{\eta} + \nabla \boldsymbol{v} : \boldsymbol{\eta} \otimes \boldsymbol{v} - p \nabla \cdot \boldsymbol{\eta} + \frac{1}{\mathrm{Re}} \nabla \boldsymbol{v} : \nabla \boldsymbol{\eta}\big) dx \\ &- \int_\Omega \frac{K}{\mathrm{ReCa}} \Big(\mu \nabla \varphi + \frac{2}{\varepsilon} W(\varphi) \nabla \gamma(u)\Big) \cdot \boldsymbol{\eta} dx, \ \forall \boldsymbol{\eta} \in H^1(\Omega)^d, \end{aligned} \tag{4.16}$$

where d is the dimension and the unknown fields are the velocity $\boldsymbol{v}$ and the pressure p. The force arising from the interfacial tension is encoded in the last term of the momentum equation. It is given in terms of an order parameter φ and a corresponding chemical potential μ which are subject to the following weak advected Blowey-Elliott Cahn-Hilliard variational inequality:

$$0 = \int_\Omega \Big(\big(\partial_t \varphi + \boldsymbol{v} \cdot \nabla \varphi\big)\psi + \frac{\mathcal{M}(\varphi)}{\mathrm{Pe}_\varphi} \nabla \mu \cdot \nabla \psi\Big) dx, \ \forall \psi \in H^1(\Omega), \tag{4.17}$$

$$0 \leq \int_\Omega \Big(- \mu(\xi - \varphi) + \varepsilon \gamma(u) \nabla \varphi \cdot (\nabla \xi - \nabla \varphi) + \frac{\gamma(u)}{\varepsilon} W'(\varphi)(\xi - \varphi)\Big) dx, \ \forall \xi \in \mathcal{K}. \tag{4.18}$$

The constants appearing in the above systems are the Reynolds number Re, the capillary number Ca, the Peclet number Pe_φ of the order parameter, and a numerical constant $K > 0$ of order one required for calibration reasons and depending only on the choice of the double-well potential (for our choice (4.3) we have that $K = 2/\pi$). The

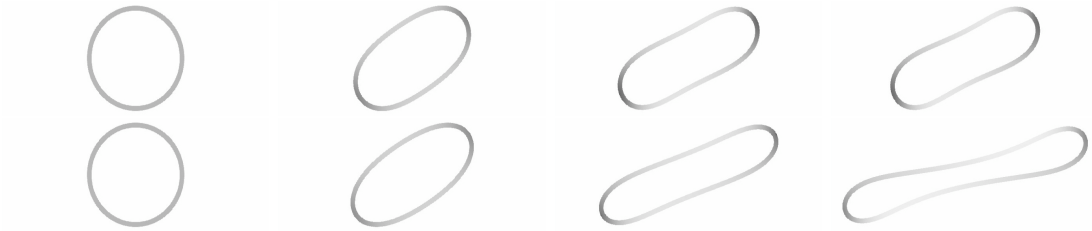

Figure 6: Diffuse interface with surfactant in two-phase flow at times $t = 0, 2, 6, 14$. In the upper line the (dimensionless) surface tension is $\sigma = 1$, in the lower line we have $\sigma(u) = 1 - u/4$. The grey scales linearly with the density ranging from 0.0 to 3.0.

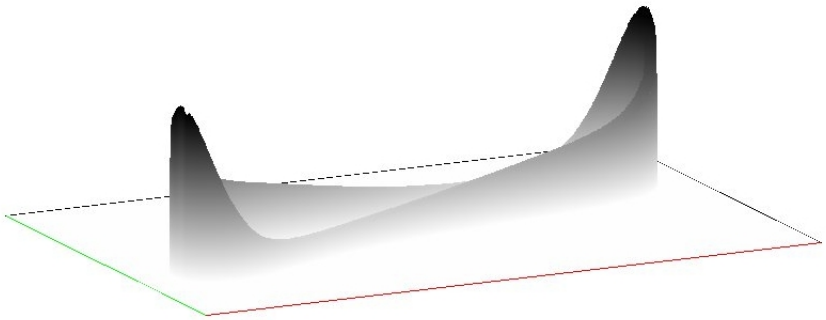

Figure 7: Diffuse interface with surfactant in two-phase flow at time $t = 14$, simulation for $\gamma(u) = 1 - u/4$. The height and the grey scales linearly with the density ranging from 0.0 to 3.0.

mobility $\mathcal{M}(\varphi)$ vanishes in the pure fluids in order to avoid diffusion from small fluid blobs to larger ones, i.e. $\mathcal{M}(\pm 1) = 0$. The surface tension $\gamma(u)$ depends on the concentration u of the surfactant which is the essential difference to the governing equations in [12].
In addition to the above systems the surfactant concentration u is subject to an equation of the form (2.1) where the velocity field $\boldsymbol{v}$ emerging from the Navier-Stokes system enters and where we set $\rho = W(\varphi)$. We remark that, in contrast to the previous application, in general, there will be advection of the surface quantity along the interface, namely, the velocity field $\boldsymbol{v}$ involves tangential components.
Using formal methods (cf. [27]) the limiting system obtained as $\varepsilon \searrow 0$ can be derived. It is characterised by two fluid phases Ω^+, Ω^- on which the Navier-Stokes system

$$\nabla \cdot \boldsymbol{v} = 0,$$
$$\partial_t \boldsymbol{v} + (\boldsymbol{v} \cdot \nabla)\boldsymbol{v} = -\nabla p + \frac{1}{\mathrm{Re}} \Delta \boldsymbol{v}$$

holds. The phases are separated by a moving hypersurface Γ transported with the flow such that the conditions

$$[\boldsymbol{v}]_-^+ = 0, \quad \boldsymbol{v} \cdot \boldsymbol{\nu}_s = v_\Gamma,$$
$$\Big[-p\boldsymbol{I} + \frac{2}{\mathrm{Re}} D(\boldsymbol{v}) \Big]_-^+ \boldsymbol{\nu}_s = -\frac{1}{\mathrm{ReCa}} \big(\gamma(u) H \boldsymbol{\nu}_s + \nabla_\Gamma \gamma(u) \big) \tag{4.19}$$

are satisfied where $\boldsymbol{\nu}_s$ is the unit normal pointing into Ω^+, H is the mean curvature of Γ, v_Γ is the normal velocity of Γ in this direction, and $D(\boldsymbol{v}) = \frac{1}{2}(\nabla \boldsymbol{v} + (\nabla \boldsymbol{v})^T)$. We remark that for obtaining (4.19) the correct choice of K is necessary, and it is essential that the mobility function $\mathcal{M}(\varphi)$ is degenerate, c.f. [1, 27]. Finally, the limiting equation for the surfactant indeed is (1.1).

To numerically approximate and solve (4.15)–(4.18) we applied the methods described in [10, 5, 34]. In particular, the saddle point problem arising from the Navier-Stokes system has been solved with a preconditioned GMRES method. The discrete Blowey-Elliott Cahn-Hilliard variational inequality (4.18) was solved with a Gauss-Seidel type iteration in which the phase field variable and chemical potential at a grid point are solved for simultaneously, [24, 5, 6]. Because of the degenerate mobility the solution is restricted to a narrow band outside of which the phase field variable is ± 1.

On the domain $\Omega = [-5, 5] \times [-2, 2] \subset \mathbb{R}^2$ the velocity was initialised at $t = 0$ with the shear flow $\boldsymbol{v}(x_1, x_2) = (x_2/2, 0)$ which also are the boundary values at later times on $\partial\Omega$. We further defined $\varphi(\boldsymbol{x}, 0) = \psi(\|\boldsymbol{x}\|_2/\varepsilon)$ with ψ as in (4.9) and $\varepsilon \approx 2\sqrt{2}/100$ which yields a circular diffuse interface of radius 1 and centre $\boldsymbol{m} = (0, 0)$. On the thin layer we initialised u homogeneously with one. The other parameter values were $\mathrm{Pe}_\varphi = 1$, $\mathrm{Re} = 10$, $\mathrm{Ca} = 0.7$ and $\mathcal{D}_c = 10$. We will report on two simulations differing in the choice of γ. In one simulation it is constant and set to one so that the surface quantity u does not influence the two-phase flow. In another simulation we set $\gamma(u) = 1 - u/4$. Starting from a uniform triangulation the grid was adaptively refined to ensure at least 8 nodes across the diffuse interface but keeping it quite coarse in the pure phases. We had a minimal edge length of $h_{\min} = 2^{-6.5} \approx 0.01105$ in the narrow band while $h_{\max} = 2^{-3} = 0.125$ in the bulk. The timestep for the phase field and surface quantity was $\tau_{CHS} = h_{\min}/(25\|\boldsymbol{v}\|_{\max}) \approx 0.000441$ whilst the Navier-Stokes system was solved with timestep $\tau_{NS} = h_{\max}/(12.5\|\boldsymbol{v}\|_{\max}) = 0.01$.

Figure 6 displays the diffuse interface in terms of the surfactant u in the range 0 (white) to 3 (black). For constant $\gamma = 1$ (first line) we observe a behaviour as in [35], Section 4.2, Figure 1. In the case $\gamma(u) = 1 - u/4$ (second line in Figure 6) the elongation of the droplet is enhanced as expected. The surfactant reveals an aggregation phenomenon at the tips of the droplet as can be seen in Figure 7. Since the surfactant lowers the surface tension the high curvature in the tips is less able to prevent the droplet from further extending by following the flow.

The dependence of the droplet shape on the thickness parameter ε and the choice of $\gamma(u)$ will be subject of future studies [27].

Additional note

In revision we learnt of the paper [51] which considers a similar approach to that of this paper using a phase field function which does not have compact support.

Acknowledgement

The second author thanks the German Research Foundation (DFG) for the financial support under Grant No. Sti 579/1-1,2. This research has been supported by the EPSRC grants EP/D078334/1(third and fourth authors) and EP/G010404 (first and second authors).

References

[1] H. Abels and M. Röger, *Existence of weak solutions for a non-classical sharp interface model for a two-phase flow of viscous, incompressible fluids*, Tech. Rep. 71, MPI Leipzig, 2008.

[2] D. Adalsteinsson and J. A. Sethian, *Transport and diffusion of material quantities on propagating interfaces via level set methods*, Journal of Computational Physics, 185 (2003), pp. 271–288.

[3] J. Barrett and C. M. Elliott, *A finite element method for solving elliptic equations with Neumann data on a curved boundary using unfitted meshes*, IMA J. Numer. Anal., 4 (1984), pp. 309–325.

[4] ——, *Finite element approximation of elliptic equations with Neumann or Robin condition on a curved boundary*, IMA J. Numer. Anal., 8 (1988), pp. 321–342.

[5] J. W. Barrett, J. F. Blowey, and H. Garcke, *Finite element approximation of the Cahn–Hilliard equation with degenerate mobility*, SIAM Journal on Numerical Analysis, 37 (1999), pp. 286–318.

[6] J. W. Barrett, R. Nürnberg, and V. M. Styles, *Finite element approximation of a phase field model for void electromigration*, SIAM J. Numer. Anal., 42 (2004), pp. 738–772.

[7] M. Bertalmío, L.-T. Cheng, S. J. Osher, and G. Sapiro, *Variational problems and partial differential equations on implicit surfaces*, J. Comput. Phys., 174 (2001), pp. 759–780.

[8] L. Blank, H. Garcke, L. Sarbu, and V. Styles, *Primal-dual active set methods for allen-cahn variational inequalities with non-local constraints*, tech. rep., University of Sussex, 2009.

[9] J. F. Blowey and C. M. Elliott, *The Cahn–Hilliard gradient theory for phase separation with non–smooth free energy part i: Mathematical analysis*, European J. Applied Mathematics, 2 (1991), pp. 233–280.

[10] ——, *The Cahn–Hilliard gradient theory for phase separation with non–smooth free energy part ii: Numerical analysis*, European J. Applied Mathematics, 3 (1992), pp. 147–179.

[11] ——, *Curvature dependent phase boundary motion and parabolic obstacle problems*, in Degenerate Diffusion, W.-M. Ni, L. A. Peletier, and J. L. Vasquez, eds., vol. 47 of IMA Volumes in Mathematics and Its Applications, Springer-Verlag, 1993, pp. 19–60.

[12] F. Boyer, *A theoretical and numerical model for the study of incompressible mixture flows*, Comp Fluids, 31 (2002), pp. 41–68.

[13] G. Caginalp, *Stefan and Hele-Shaw type models as asymptotic limits of the phase field equations*, Phys. Rev. A, 39 (1989), pp. 5887–5896.

[14] X. Chen and C. M. Elliott, *Asymptotics for a parabolic double obstacle problem*, Proc. Roy. Soc. London Ser. A, 444 (1994), pp. 429–445.

[15] K. Deckelnick, G. Dziuk, and C. M. Elliott, *Computation of geometric partial differential equations and mean curvature flow*, Acta Numerica, 14 (2005), pp. 139–232.

[16] K. Deckelnick, G. Dziuk, C. M. Elliott, and C.-J. Heine, *An h-narrow band finite-element method for elliptic equations on implicit surfaces*, IMA Journal of Numerical Analysis, (2009/3/4), pp. drn049–.

[17] K. Deckelnick, C. M. Elliott, and V. Styles, *Numerical diffusion-induced grain boundary motion*, Interfaces Free Bound., 3 (2001), pp. 393–414.

[18] G. Dziuk, *Finite elements for the Beltrami operator on arbitrary surfaces*, in Partial differential equations and calculus of variations, S. Hildebrandt and R. Leis, eds., vol. 1357 of Lecture Notes in Mathematics, Springer Berlin Heidelberg New York London Paris Tokyo, 1988, pp. 142–155.

[19] G. Dziuk and C. M. Elliott, *Finite elements on evolving surfaces*, IMA Journal Numerical Analysis, 25 (2007), pp. 385–407.

[20] ——, *Surface finite elements for parabolic equations*, J. Comput. Math., 25 (2007), pp. 385–407.

[21] ——, *Eulerian finite element method for parabolic pdes on implicit surfaces*, Interfaces and Free Boundaries, 10 (2008), pp. 119–138.

[22] ——, *An Eulerian approach to transport and diffusion on evolving implicit surfaces*, Computing and Visualization in Science, 13 (2010), pp. 17–28.

[23] C. Eilks and C. M. Elliott, *Numerical simulation of dealloying by surface dissolution via the evolving surface finite element method*, Journal of Computational Physics, 227 (2008), pp. 9727–9741.

[24] C. M. Elliott and A. R. Gardiner, *One dimensional phase field computations*, in Numerical analysis 1993, D. F. Griffiths and G. A. Watson, eds., vol. 303 of Pitman Rearch Notes in Mathematics Series, Longman Scientific and Technical, 1994, pp. 56–74.

[25] C. M. Elliott and B. Stinner, *Analysis of a diffuse interface approach to an advection diffusion equation on a moving surface*, Math. Mod. Meth. Appl. Sci., 19 (2009), pp. 1–16.

[26] ——, *Modelling and computation of two phase geometric biomembranes using surface finite elements*, Submitted, (2009).

[27] C. M. Elliott, B. Stinner, and V. Styles, *Diffuse interface modelling of surfactants in two-phase flow*, in preparation, (2009).

[28] C. M. Elliott and V. M. Styles, *Computations of bidirectional grain boundary dynamics in thin metallic films*, J. Comp. Phys., 187 (2003), pp. 524–543.

[29] P. C. Fife, J. W. Cahn, and C. M. Elliott, *A free-boundary model for diffusion-induced grain boundary motion*, Interfaces Free Bound., 3 (2001), pp. 291–336.

[30] C. Gräser and R. Kornhuber, *Multigrid methods for obstacle problems*, J. Comp. Mathematics, 27 (2009), pp. 1–44.

[31] J. B. Greer, *An improvement of a recent Eulerian method for solving PDEs on general geometries*, J. Sci. Comput., 29 (2006), pp. 321–352.

[32] J. B. Greer, A. L. Bertozzi, and G. Sapiro, *Fourth order partial differential equations on general geometries*, J. Comput. Phys., 216 (2006), pp. 216–246.

[33] A. J. James and J. Lowengrub, *A surfactant-conserving volume-of-fluid method for interfacial flows with insoluble surfactant*, Journal of Computational Physics, 201 (2004), pp. 685–722.

[34] D. A. Kay, V. Styles, and R. Welford, *Finite element approximation of a Cahn-Hilliard -Navier-Stokes system*, Interfaces and Free Boundaries, 10 (2008), pp. 15–43.

[35] M.-C. Lai, Y.-H. Tseng, and H. Huang, *An immersed boundary method for interfacial flows with insoluble surfactant*, Journal of Computational Physics, 227 (2008), pp. 7279–7293.

[36] J. Lowengrub, J.-J. Xu, and A. Voigt, *Surface phase separation and flow in a simple model of multicomponent drops and vesicles*, Fluid Dynamics and Matrial Processing, 3 (2007), pp. 1–20.

[37] C. B. Macdonald and S. J. Ruuth, *Level set equations on surfaces via the Closest Point Method*, Journal of Scientific Computing, 35 (2008), pp. 219–240.

[38] ——, *The implicit closest point method for the numerical solution of partial differential equations on surfaces*, SIAM Journal on Scientific Computing, 31 (2009), pp. 4330–4350.

[39] U. F. Mayer and G. Simonett, *Classical solutions for diffusion-induced grain-boundary motion*, J. Math. Anal. Appl., 234 (1999), pp. 660–674.

[40] R. H. Nochetto, M. Paolini, and C. Verdi, *Optimal interface error estimates for the mean curvature flow*, Ann. Scuola Norm. Sup. Pisa, 21 (1994), pp. 193–212.

[41] M. A. Olshanskii and A.Reusken, *A finite element method for surface pdes: matrix properties*, Numerische Mathematik, 114 (2010), pp. 0945–3245.

[42] M. A. Olshanskii, A. Reusken, and J. Grande, *A finite element method for elliptic equations on surfaces*, SIAM J. Numer. Anal., 47 (2009), pp. 339–3358.

[43] S. Osher and R. Fedkiw, *Level set methods and dynamic implicit surfaces*, vol. 153 of Appl. Math. Sci, Springer Verlag, 2003.

[44] A. Rätz and A. Voigt, *Pde's on surfaces - a diffuse interface approach*, Communications in Mathematical Sciences, 4 (2006), pp. 575–590.

[45] S. J. Ruuth and B. Merriman, *A simple embedding method for solving partial differential equations on surfaces*, Journal of Computational Physics, 227 (2008/1/10), pp. 1943–1961.

[46] A. Schmidt and K. G. Siebert, *Design of adaptive finite element software: The finite element toolbox ALBERTA*, vol. 42 of Lecture notes in computational science and engineering, Springer, 2005.

[47] P. Schwartz, D. Adalsteinsson, P. Colella, A. P. Arkin, and M. Onsum, *Numerical computation of diffusion on a surface*, Proceedings of the National Academy of Sciences, 102 (2005), pp. 11151–11156.

[48] J. A. Sethian, *Level set methods and fast marching methods,*, vol. 3 of Cambridge Monographs on Applied and Computational Mathematics, Cambridge University Press, 1999.

[49] C. Stöcker and A. Voigt, *Geodesic evolution laws—a level-set approach*, SIAM Journal on Imaging Sciences, 1 (2008), pp. 379–399.

[50] ——, *A level set approach to anisotropic surface evolution with free adatoms*, SIAM Journal on Applied Mathematics, 69 (2008), pp. 64–80.

[51] K. E. Teigen, X. Li, J. Lowengrub, F. Wang, and A. Voigt, *A diffuse-interface approach for modelling transport, diffusion and adsorption/desorption of material quantities on a deformable interface*, Communications in Mathematical Sciences, 7 (2009), pp. 1009–1037.

[52] J.-J. Xu and H.-K. Zhao, *An Eulerian formulation for solving partial differrential equations along a moving interface*, Journal of Scientific Computing, 19 (2003), pp. 573–594.